TECHNISCHE UNIVERSITÄT WIEN

MASTER THESIS

(W,Mo)C-based cemented carbides with alternative binder phase

Vienna University of Technology
Institute of Chemical Technologies and Analytics
Getreidemarkt 9/164−CT
1060 Vienna

under the supervision of
Ao. Univ.Prof. Dipl.-Ing. Dr.techn. Walter LENGAUER
Dipl.-Ing. Markus FÜRST B.Sc.

Georg HATZL, BSc
Großer Ring 8
1130 Wien

Technische Universität Wien
Wien, 22. October 2021

Abstract

(W,Mo)C-based cemented carbides with Ni-based binders were investigated for the following two reasons. On the one hand, Co is a critical element for economic and health concern reasons. Therefore, it is of great interest for the hardmetal sector to reduce or completely avoid the consumption of this element in the future. On the other hand, the aim was to reduce the tungsten content in cemented carbides by substituting it with molybdenum. Molybdenum is the only element that is soluble in WC in significant quantities without changing the crystal structure. In this work (W,Mo)C hardmetals have been investigated with Ni-based binders (pure Ni and 85Ni15Fe with and without Cr_3C_2 as grain-growth inhibitor), changing two parameters of the common WC-Co system. The hard-phase powders were of composition $(W_{0.91}Mo_{0.09})C$ with an average grain size of 1.2 µm and $(W_{0.76}Mo_{0.24})C$ and with average grain sizes of around 0.5 and 1.3 µm, respectively. In addition, a hardmetal grade with individual WC and Mo_2C powders grade was prepared with a Mo content corresponding to that of the $(W_{0.91}Mo_{0.09})C$ grade. All starting formulations had the same nominal amount of binder phase. The sintering was conducted in a low-pressure Ar atmosphere. Properties such as porosity, microstructure evolution, hardness and fracture toughness were investigated and compared to (W,Mo)C hardmetals with Co binder. As a result, it was possible to produce hardmetals with acceptable quality, that were investigated for their sintering behaviour and their material properties with metallography, SEM, DTA, Dilatometry, Powder-XRD and hardness/fracture toughness. This new category of cemented carbides turned out to be chemically challenging regarding the sintering process as the unique interaction of each hard and binder phase leads to mixed results. The use of the softer Ni as a binder base resulted in a significant loss in hardness but equal gains in the fracture toughness. The use of ultra-fine (W,Mo)C powders improves the hardness to a point that is comparable or even succeeding that, of the common WC-Co system. However, one of the pre-alloyed powders is plagued with low sintering activity resulting in high residual porosity. This means that further optimisation of the microstructure, e.g. by doping with other carbide formers is still necessary, to utilize the full potential of the (W,Mo)C solid solution. Nevertheless, it is possible to achieve similar properties as the common materials - with ca. 25% less consumption of W and without the use of Co.

Table of Content

1 INTRODUCTION

1.1 Topics of this work

Cemented carbides or hardmetals are an essential material in industry and construction [1]. In current times, the exceptional material properties of cemented carbides made them indispensable [1], however, they have come under criticism because of their use of Cobalt. Cobalt, the main component of the binder, was put on the list of critical resources by the EU [2]. It is an important element for electronics and battery technology, an industry that will certainly continue to grow in the coming years. This led to a steady increase in demand and price for this element while the demand for cemented carbides is also increasing [1, 3]. In addition to the critical situation of the raw material supply, there are also political concerns about mining conditions, as the cobalt mines in D.R. Congo, which is responsible for 70 % of the worldwide cobalt production in 2020 [4], have long been known for their contemptuous working methods [5]. There are some good reasons to research alternatives for Cobalt in the production of cemented carbides. However, since its discovery about 100 years ago, the combination of tungsten carbide (WC) and cobalt is almost perfect. Despite numerous attempts to find an alternative, it turned out that the optimal system was used from the beginning. [1]

However, it is not only the components for the binder that are threatened by availability: in the mid-1970s there was a significant increase in tungsten prices on the world market [6]. Alternatives were sought and research on (W,Mo)C-based hardmetals has begun [7-9]. According to today's knowledge, molybdenum is the only element that can completely dissolve in the hexagonal structure of WC [7-9]. This makes it effectively possible to reduce tungsten consumption without considerably weakening the mechanical properties of the finished hardmetal [10]. Years later the markets calmed down again and most of the research in this area was subsequently discontinued and was resumed a few years ago [11-14]. China has by far the largest tungsten reserves in the world with an estimated 1.9 million tonnes and is accounted for 85 % of global tungsten production in 2020 [4, 15]. This means that China dominates the tungsten market, which is not viewed uncritically, although there is no reason for concern so far. After all, China also has to import a lot of tungsten due to the increasingly poor quality of the raw materials and the lack of processing options [15]. Furthermore, tungsten is a strategic resource, as it is used for armour-piercing ammunition due to its high density. In 2017, 6 % of global tungsten consumption was allocated to the defence sector [4]. Thus, there is always the possibility in the future that, depending on the political situation and military activity, the demand could also rise sharply resulting in price spikes. In this case, it would be practical to easily reduce the tungsten content of the cemented carbides with the cheaper molybdenum to prevent an increase in end-product prices.

This work is one of the first in a long time to produce and investigate both alternatives of the classic cemented-carbide system: a cobalt-free binder system and reduced tungsten content. Four different (W,Mo)C-carbide phases with different Mo content, grain size and production methods are investigated. Three of these powders are pre-alloyed powders produced by Global Tungsten & Powder, USA, which are compared to a powder mixture of WC and Mo_2C-powders, the common method to produce (W,Mo)C hardmetals on a laboratory scale to date. For the binder phase, two different systems are tested. One is a pure Ni-binder and the other is a Ni-Fe alloy with 85 % nickel and 15 % iron. Both systems will be produced one time each with 0.5 wt% Cr_3C_2 as a grain-growth inhibitor. The aim is to use this new combination of hard phase and binder to produce two-phase, pore-free cemented carbides and to compare the results with the (W,Mo)C-Co hardmetals investigated by Schwarz et. al. [11, 12] and the classic WC-Co cemented carbides.

1.2 Theoretical background

1.2.1 Introduction to cemented carbides

Hardmetals or cemented carbides can be defined as:

> *"…powder metallurgical, liquid-phase sintered composite materials consisting of at least one hard and wear-resistant phase; in the majority of cases, this being tungsten carbide (WC), and a ductile and softer metallic phase from the iron group of metals."* [1]

Both terms are equal and only differ in their regional use.

The patent for hardmetals was applied for in 1923 by Karl Schröter to produce wire drawing tools. Quite quickly, however, cemented carbides were used primarily for tipped or cutting tools for the machine tool industry [1]. A hardmetal is characterised by its exceptional hardness, stiffness and compressive strength combined with relatively high toughness and wear resistance. Furthermore, the high-temperature resistance is excellent, especially because the thermal conductivity is about twice as high as that of high-speed steel [1]. These properties ensure that hardmetals are nowadays also used for mill rolls, punching tools, dies, drill heads and industrial nozzle heads (e.g. sandblasting or high-pressure water jets) [1]. The biggest disadvantage of this material is its high density (up to 15 g/cm³), which rules it out for some applications.

1.2.1.1 Role of the Binder

The properties of hardmetals are mainly determined by the binder content, the grain size of the hard phase and the C content. The binder content typically ranges between 2-30 wt% and fulfils two tasks: Strengthening and cementing the WC grains as well as introducing ductility and toughness into the otherwise brittle hard-material particles [1]. The most commonly used binder is cobalt because it wets WC perfectly, has the best mechanical properties of all the iron-group metals and, thanks to its ferromagnetic properties, allows the C content to be determined non-destructively by measuring the coercivity. Ni or Fe-based binders have been researched but are still niche products: Ni-based binders are mainly suitable for use in acid-corrosive conditions and Fe-based binders are used for wood cutting tools. In general, however, the tool properties of these systems are worse than those with Co. So far, the most successful system for reducing the Co content is the FeCoNi-binder system, which can match or sometimes even outperform pure Co. Smaller grain sizes can compensate for the inferior material properties of alternative binders, however, these are harder to synthesise [1].

1.2.1.2 Role of the Grain size

Possible grain sizes are defined in Table 1-1. There is a wide range of carbide formers (e.g. Ta, Ti, Cr and Mo) that can be used as grain-growth inhibitors, effectively reducing the grain size after sintering. Changes in these parameters primarily influence hardness, toughness and abrasive wear resistance. [1] The hard phases used in this work thus fall into the category's submicron to fine.

Table 1-1: Classification of hard-phase grain sizes according to Mari et al. [1]

Grain Size (µm)	Designation
<0.2	Nano
0.2- 0.5	Ultrafine
0.5- 0.8	Submicron
0.8- 1.3	Fine
1.3- 2.5	Medium
2.5- 6.0	Coarse
>6.0	Extra coarse

1.2.2 Synthesis of cemented carbides

Cemented carbides are produced by powder metallurgy. Hence, the starting materials are metal powders that are pressed into the desired shape (green shaping) and then sintered into a solid-metallic material. The advantage over the casting method is that certain alloys and composite materials can be produced that otherwise would not form a solution in the melt or the melting points are too high to be accessible through metal casting. Sintering generally means solidification below the melting point by diffusion, i.e. without the appearance of a liquid phase. Furthermore, the pressing of green compacts allows more complicated shapes and a near-net-shape production of tools without the need for significant post-processing [1].

During sintering, the composite material is formed from a WC- and binder-powder mixture. For the production of cemented carbides, so-called liquid-phase sintering (LPS) is used. In contrast to normal sintering methods, a liquid phase is present, increasing the sintering activity of the system. For cemented carbides, at temperatures between 1400° and 1500°C the metallic binder melts and spreads between the still solid hard-material particles and closes pores. The aim of sintering hardmetals is a fully dense material without residual porosity.

The liquid binder not only arranges the hard-material particles but also dissolves a certain amount of the carbides. How much the binder can dissolve depends on the C content and the additives of the system. Unique for LPS is the so-called solution-reprecipitation process [1]. Some of the solid material of the hard phase dissolves in the liquid binder, diffuses to a different location and precipitates again as a solid, promoting grain growth. After the liquid has reached saturation, the solid grains in contact with each other grow sinter bonds, creating a rigid three-dimensional solid skeleton structure in whose interstices the liquid is dispersed [1]. This process of precipitation on large grains gives the hard-material grains their characteristic prismatic shape, which is due to the hexagonal crystal structure of WC [16].

The determining driving force for sintering is the reduction of the surface, or more precisely, the lowering of the surface energy. For liquids and solids, a surface is always an energetically unfavourable area, since the atoms and molecules on the surface have fewer binding partners. As a result, they always strive towards the interior and, conversely, must perform work when they diffuse to the surface (Figure 1-1). The amount of work (ΔW) in relation to the area formed (ΔA) is the surface energy (γ) (Equ. 1-1) [17]. Matter and liquids therefore always strive to have the smallest possible surface energy.

$$\gamma = \frac{\Delta W}{\Delta A} \left[\frac{J}{m^2} = \frac{N}{m}\right] \qquad \text{Equation 1-1}$$

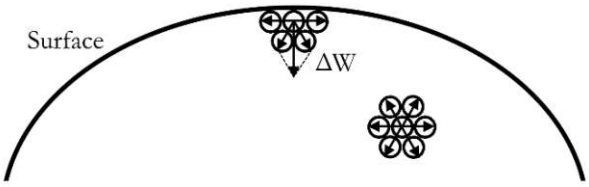

Figure 1-1: Schematics for the surface energy [17]

A densely packed green body consists of many small particles or grains with a large surface area in relation to their volume. The driving force of sintering is the reduction of the surface area, which means that smaller grain sizes result in a higher sinter activity.

1.2.2.1 Complications of sintering cemented carbides

Sintering is a process based on diffusion, i.e. mass transport in solid phases. To move an atom in a crystal lattice, it has to be detached from its bond neighbours. How easily this can be done depends on the absolute melting point of the compound. High melting substances such as carbides and nitrides have high binding energies and therefore require high temperatures for sintering. LPS facilitates the sintering of these high-melting substances in that a molten binder partially dissolves the hard phase and therefore wets it perfectly, which considerably increases the diffusion rate. This also creates capillary forces that pull the grains together at up to 10 atm [1] and thus significantly increases the sintering efficiency. In this way, sintering can already take place at substantially lower temperatures.

Pore elimination is a crucial aspect of sintering cemented carbides. Pores are voids in the microstructure that drastically degrade the mechanical properties of the material. During LPS the capillary forces ensure that the small pores are filled first, which in turn leads to ab increase of the average pore-size, while the number of pores decreases. This coarsening of the pores acts against densification, especially when sintering gases are produced. This can be prevented by vacuum sintering or applying high external pressure (HIP) [1].

Another complication is the adjustment of the C content. C reacts with W to form the intermetallic phase WC, while excess C is absorbed into the binder phase. If too much C is present to be fully absorbed, the C will

accumulate as free graphite in the microstructure. However, if the C content is too low, eta-phase (η-carbides) is formed. It is necessary to lower or increase the C content through doping of additional C or W to reach the narrow two-phase region, otherwise, the material properties of the cemented carbides will be compromised. [1] Each specimen has to be adjusted individually since the C content of the final sample is influenced by adsorbed O_2 and moisture of the starting powders. However, the check for additional phases can only take place after sintering. As a result, doping can become a time-consuming process, especially on a laboratory scale. [1]

The C content also influences the onset of the liquid-phase formation of the binder during LPS. The [M_6C|WC|Co_{fcc}|Co_{liquid}] and the [Free C|WC|Co_{fcc}|Co_{liquid}] equilibria are invariant, i.e. the liquid-phase formation temperature of the binder is consistent within each region. These temperatures are therefore used as a reference for the differential thermal analysis, used to investigate cemented-carbide specimens.

1.3 The (W,Mo)C hard phase

The first experiments on the substitution of W with Mo began as early as the mid-1970s, as a rapid increase in tungsten prices at that time [6] motivated a technical solution. The idea was to replace large parts of the tungsten in hardmetals with cheaper Mo. In a detailed study, Schuster et al. [8] were able to confirm the complete solubility of MoC in WC. A solid solution with (W,Mo)C is formed, whereby the Mo content can be varied as desired. The research was aimed to produce new cemented carbides with this solid solution and therefore effectively reducing the W consumption for cemented carbides.

Schuster et al. [8] also investigated changes in the lattice parameters of the hexagonal structure. With increasing Mo content, the c-lattice parameter changes from 2.837 Å to 2.830 Å at 20 at% Mo (Figure 1-2). Conducting tempering experiments at 1190°C and 1230°C with these newly found (W,Mo)C solid solutions, Schuster and his colleagues were able to show that the phase $(W,Mo)_2C$ also appears in the microstructure as soon as the Mo content rises above 40 at%.

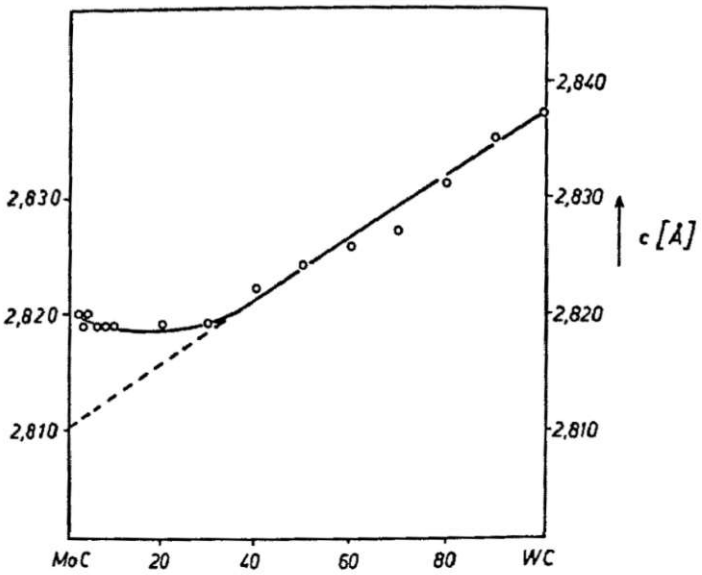

Figure 1-2: Changes to the c-lattice parameter depending on the Mo content in the (W,Mo)C solid solution taken from Schuster et al. [8]

In 1977, Yih et al. [9] filed a patent for cemented carbides with hexagonal MoC, with detailed thermodynamical information (Figure 1-3 and Figure 1-4, page 6) and additionally included the first detailed application test of such cemented carbides. They mainly investigated Mo contents above 50 at% with a binder phase containing iron-group metals. Relevant for the present work, Ni binders and the addition of Cr to the binder were investigated too, with the result that the Ni binder is better suited for cutting tools, as they generate less friction and thus less wear. The addition of Cr in their tests reduced toughness and strength but increased oxidation resistance. Hence, no detailed or quantitative information on these results was given in the patent. A wide range

of different systems was patented, and overall, the results can be summarised, as follows: Cemented carbides on a (W,Mo)C basis, coated and uncoated, perform equally well as Mo-free cemented carbides.

1.3.1 Thermodynamic investigation of the W-Mo-C system

To understand why molybdenum is used to substitute tungsten in the hard phase, consider the partial Mo-W-C ternary phase diagram at 1450°C shown in Figure 1-3. The unique interaction between WC and Mo is represented by the horizontal line in the middle of the diagram, indicating a continuous solid solution (W,Mo)C (labelled ε-phase in Figure 1-3 and Figure 1-4). Starting from the right at the point of 50 at% C, this line indicates how much Mo can be added to the intermetallic WC phase without changing its structure. The lattice parameters of hexagonal MoC deviate minimally from the WC structure [8], which creates this broad solubility. It is possible to replace W up to a proportion of 85 at% Mo at this temperature.

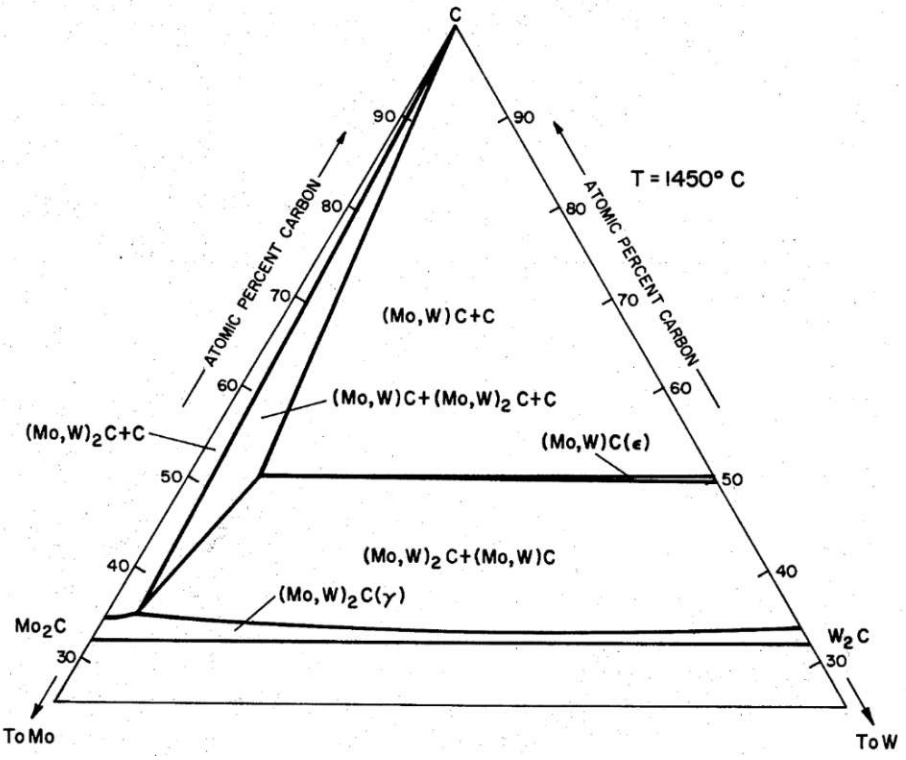

Figure 1-3: Ternary phase diagram of W-Mo-C at 1450°C taken from Yih et al. [9]

Figure 1-4 shows the isopleth along the (W,Mo)C section of the phase diagram, showing the stability of this solid solution at different temperatures. At lower temperatures, the solid solution extends to the binary MoC. The pure MoC phase is only stable up to 1180°C. At higher temperatures, the monocarbide solution decomposes into $(Mo,W)_2C$ (γ) and free C. The stability increases rapidly with rising Mo content. This means the targeted monocarbide phase is a low-temperature phase. In reality, mixing Mo_2C and C and tempering it for hundreds of hours at the appropriate temperatures will not yield any MoC [9]. However, it is possible to create the hexagonal monocarbide phase by cooling the cubic α-phase $(Mo,W)C_{1-X}$ and the pseudo cubic η-phase $(Mo,W)_3C_2$ because of the short diffusion paths of the C, increasing the chemical kinetics [9]. The diffusion can be accelerated even more by the addition of iron-group of metals (Fe, Co and Ni) and the use of LPS, relevant for the synthesis of cemented carbides using the (W,Mo)C phase. Yih et al. already stated that the preferable method to synthesise the (W,Mo)C phase would be a mixture of WC, Mo_2C and graphite to compensate for the loss of C.

The system was then further explored at the time by Rudy et al. [7] and Kieffer et al. [18] always with the same result: In terms of hardness, thermal conductivity and Young's modulus the monocarbide solid solution has very similar properties to the tungsten monocarbide while at the same time having a lower density.

Metallographic investigations of actual cemented-carbide specimens reveal that this thermodynamic model of complete solid solution is still overruled by the kinetics, as no homogeneous microstructure, even with elongated tempering, is achievable [10-12].

Schubert et al. [19] investigated the thermodynamics of quaternary Co-Mo-W-C and Ni-Mo-W-C systems with 60 at% Co and Ni respectively, in foresight of their use in cemented carbides. They were able to prove the solubility between MoC and WC in these systems with DTA, metallography and x-ray methods. Akmoran et al. [20] investigated the solubility of this solid solution in the binder with the result that Mo dissolves more easily in the binder and this effect is further enhanced in Ni binders. Due to the high amount of Mo already present in the hard phases used in the present work, it can be assumed that the binder phase is saturated with Mo and thus reprecipitates as (W,Mo)C. Nevertheless, the large amount of Mo changes the interaction with the binder and other inhibitors compared to Mo-free hardmetals [12].

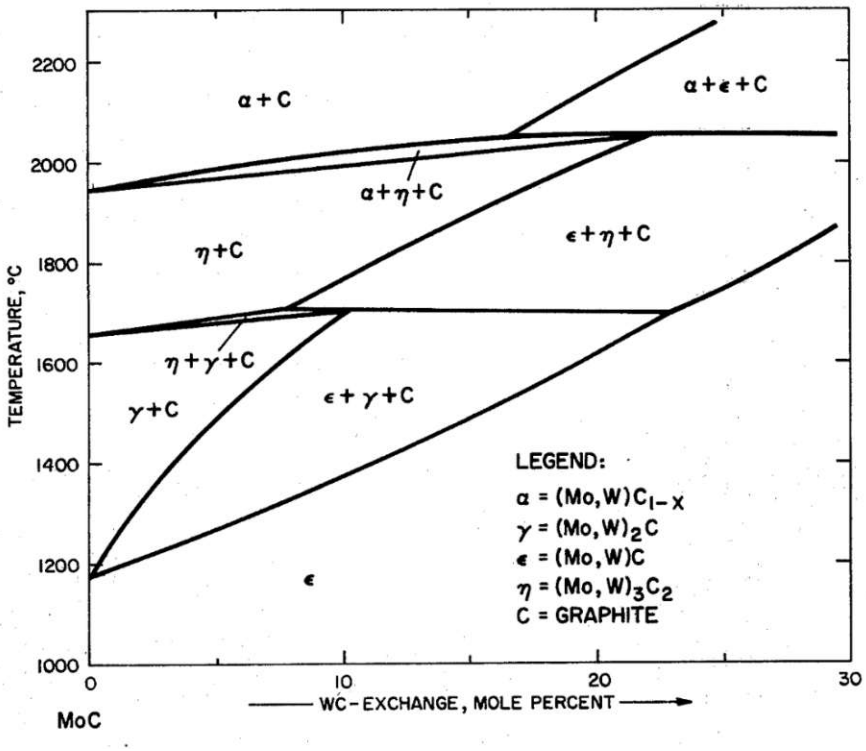

Figure 1-4: Isopleth of the Mo-W-C system along the section of MoC-WC taken from Yih et al. [9]

1.3.2 Further research

However, the findings by Yih et al. [9] remained unused by the industry, and after the tungsten price returned to normal by the mid-1980s [6] interest in using and developing these newfound cemented-carbide systems was lost. In hindsight, the research from that time cannot be fully compared with today's research, because practically all of these works focused on Mo contents from 30- 80 at%, i.e. significant higher Mo contents than used in this work.

Shortly after the beginning of the 21st century, research was resumed. Moien et al. [21] published their research with 50 at% Mo in the hard phase in 2006 and came up with very similar results as Yih et al. [9] in the late 70s. Very influential to the present work is the research of Liu et al. [10] published in 2012, who at that time did a detailed study on (W,Mo)C ceramics with different Mo contents. A powder mixture of WC, Mo_2C and graphite was used, which was processed into binder-free samples by hot pressing. At Mo contents below 20 at%, Mo_2C dissolves completely. However, this formation of a solid solution creates pores. Furthermore, the metallographic examination with the scanning electron microscope (SEM) showed that the individual grains of the solid solution were not homogeneous and formed a W-rich "core". The mechanical examination showed that the hardness of the (W,Mo)C ceramics only decreases with a Mo content of more than 20 at% (Figure 1-5, left).

This is one of the reasons why the hard phase $(W_{0.76}Mo_{0.24})C$ represents the highest Mo content in the present work. The fracture toughness of the hard phase is only marginally influenced (Figure 1-5, right).

Decisive preliminary work was done by Schwarz et al. [11, 12] who started with the investigation of (W,Mo)C with low Mo contents, the preparation of samples and the controlling of the C content to reach the two-phase region, setting a basis for the experimental procedure and results of the present work. Cemented carbides were produced from a mixture of WC, Mo_2C and graphite powder. Co was used for the binder phase. The results of the works by Schwarz et al. [11, 12] thus serve as a reference for (W,Mo)C-Co carbides and can be summarised as follows: The grains are strongly rounded in the microstructure, which was already noted by Dalbauer et al. [14] and T.J. Jewett [13]. With the help of differential thermal analysis (DTA) investigations, it was possible to determine that the melting temperature is reduced by the addition of Mo. Furthermore, mechanical tests were carried out revealing promising material properties which are used later in this work for comparison.

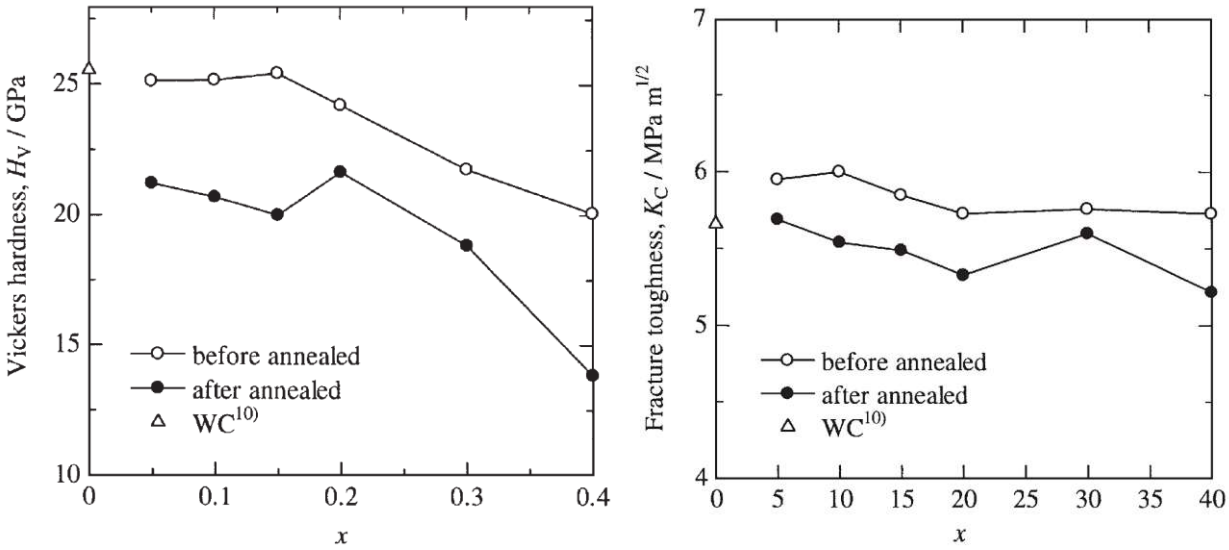

Figure 1-5: Influence of the Mo content on the hardness and fracture toughness of the (W,Mo)C ceramic phase according to Liu et al. [10]

1.3.2.1 Pre-alloyed (W,Mo)C powders

There are two possibilities for the synthesis of (W,Mo)C cemented carbides, both are used in this work:

1. A powder mixture of WC and Mo_2C powder, where the C deficit must be compensated by adding extra graphite. This is the usual procedure suggested by Yih et al. [9] and will therefore be used as a reference for one batch of specimens in the present work.
2. To simplify the synthesis there is also the possibility to pre-alloy the hard phase with the appropriate Mo content. In this work, the majority of the used hard-phase powders are pre-alloyed.

2 EXPERIMENTAL

2.1 Powders and sample composition

Four different types of (W,Mo)C hard-phase powders were employed (Table 2-1). Powders of types A to C were pre-alloyed, ternary (W,Mo)C powders manufactured industrially by GTP, Towanda, USA. The ternary powders displayed as "W5MoC" contain 5wt% Mo and are represented by the formula $(W_{0.91}Mo_{0.09})C$ and that of "W15MoC" contain 15wt% Mo with the formula $(W_{0.76}Mo_{0.24})C$. Contrary, the hard-phase powder for type D is a mixture of WC powder with 1.22 µm FSSS (Fisher Sub-sieve Sizer) grain size and Mo_2C powder with 1.49 µm FSSS grain size (both from Treibacher Industrie AG, Althofen, A). To reach the phase "MoC" solvable in the WC, carbon black (Luvocarb, H.C. Starck GmbH, Goslar, D) was added to compensate for the C deficiency of the compound Mo_2C. The same C powder was used for the C doping of the powder mixtures.

Table 2-1: Composition and grain size of the raw hard phases

Hardmetal Type Designation	Hard-phase Powder	Chemical stoichiometry	Grain size (µm)	Th. Density (g/cm³)
A	"W5MoC"	$(W_{0.91}Mo_{0.09})C$	1.2 (FSSS)	15.13
B	"W15MoC"	$(W_{0.76}Mo_{0.24})C$	1.3 (FSSS)	14.05
C	"W15MoC"	$(W_{0.76}Mo_{0.24})C$	0.5 (FSSS)	14.05
D	"WC-5MoC"	$(W_{0.91}Mo_{0.09})C$	1.22 /1.49 (FSSS)	15.28

The binder phases were pure Ni for the first and a Ni85Fe15 mixture for the second batch of samples (Ni: Speciality Metals, SA, 1.89 µm FSSS"; Fe: Yuelong GmbH, D, 3.4 µm FSSS). The amount of binder was adjusted to 16.4vol% for both batches. Additionally, both batches were repeated with an addition of 0.5 wt% (of the entire powder mixture) with Cr_3C_2 (Treibacher Industrie AG, 1.44 µm FSSS) as a grain-growth inhibitor. In total 4 sample batches were created, where the batch number represents a different binder system, creating a total of 16 samples (Table 2-2).

Table 2-2: All samples and their composition of hard phase and binder system

Batch #	Hard phase A	Hard phase B	Hard phase C	Hard phase D
1	W5MoC -Ni	W15MoC 1.3 µm -Ni	W15MoC 0.5 µm -Ni	WC-5MoC -Ni
2	W5MoC -Ni85Fe15	W15MoC 1.3 µm - Ni85Fe15	W15MoC 0.5 µm - Ni85Fe15	WC-5MoC - Ni85Fe15
3	W5MoC -Ni-Cr_3C_2	W15MoC 1.3 µm - Ni-Cr_3C_2	W15MoC 0.5 µm - Ni-Cr_3C_2	WC-5MoC -Ni-Cr_3C_2
4	W5MoC - Ni85Fe15-Cr_3C_2	W15MoC 1.3 µm - Ni85Fe15-Cr_3C_2	W15MoC 0.5 µm - Ni85Fe15-Cr_3C_2	WC-5MoC - Ni85Fe15-Cr_3C_2

2.2 Sample preparation

2.2.1 Powder milling

For the sample preparation, the powders first had to be weighed in precisely and in the correct ratio. An analytical balance (Mettler AE 200) with a resolution of 0.1 mg was used for weighing. Each batch was calculated for precisely 150 g. The weighed powders were transferred directly into the hardmetal grinding cup one after the other. The grinding balls were then carefully poured onto the powder. To prevent the powder from being stirred up, the balls were rolled into the cup in such a way that they first bounce off the wall of the cup so that

they hit the powder bed more gently. The grinding balls were made of conventional cemented carbide, had a diameter of about 4 mm and were always used in a 10:1 ratio to the metal powders. The grinding cup was now filled with the grinding medium (cyclohexane) to just below the rim. To remove the remaining air from the mass, it was carefully stirred with a spatula. Again, care was taken to stir up as little of the powder as possible. To improve this process, later batches were also given an ultrasonic cleaning. As soon as no more air bubbles were visible, the grinding cup was completely filled with cyclohexane and carefully closed to ensure that no air was trapped.

The hardmetal grinding cups were then sealed air-tight with a protective steel cage and placed on the roller mill. The first batch was ground for 24 h. As longer grinding was shown to have positive effects on porosity, the grinding time was initially increased to 48 h for the second batch, and to 72 h for batches 3 and 4. A timer was used to operate the roller mill for the specified period. After grinding, the cups were opened, the excess cyclohexane was removed and the powder slurry was separated from the grinding media with the help of a coarse sieve. To keep the loss of powder low, the grinding balls were still thoroughly rinsed with a spray bottle filled with cyclohexane. The slurry was then left to sediment for about 5 minutes and the supernatant was drawn off. The powder slurry was then dried at 70°C for 15-20 h at atmospheric pressure, finely sieved and transferred into PVC bottles. The finalised powder samples were stored in a desiccator with silica gel to protect the powders from moisture.

2.2.2 Pressing and sintering

For sintering hardmetal specimens the powders were uniaxially pressed with 155 MPa for 20 s into cylindric green bodies with a diameter of 12.8 mm and a weight of approx. 6 g. The green bodies were then measured for height and diameter and weighted again before being put into the graphite crucible.

The samples were sintered in 100 mbar Ar atmosphere at 1480°C for 1 h in a vacuum induction furnace. The sintering profile is shown in Figure 2-1 and was operated via an automatic control system. The vacuum pump was connected during the first heat-up and the first plateau. After that, the valve to the pump was closed and 100 mbar Ar gas was added. The temperature was taken with an infrared pyrometer. The profile starts at 400°C and ends at 800°C.

After the samples were cooled off, they were weighted immediately and measured again for height and diameter.

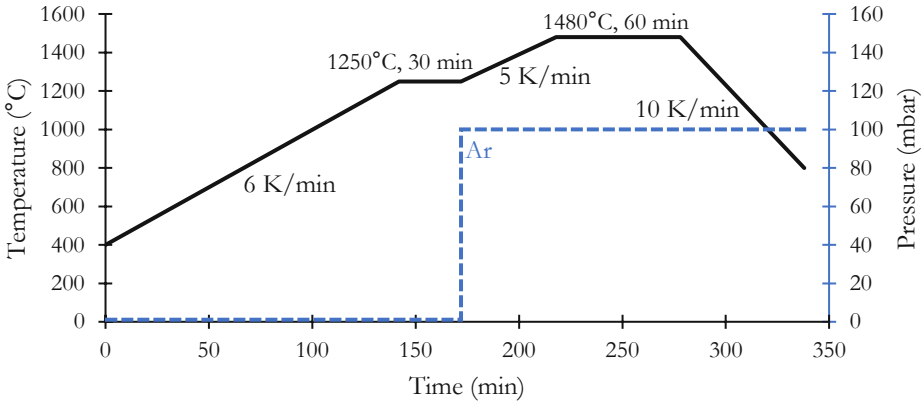

Figure 2-1: Sintering profile with heating rates and dwell specifications

2.2.3 Metallurgical sample preparation

The sintered cemented carbides were then cut in half using a Struers Accutom-10. The diamond cutting disc (A.B. Technics Handels GmbH) was operated at 3000 rpm and a feed of 0.015- 0.030 mm/s, depending on the resistance during cutting. One half was then mounted in Bakelite using a Struers CitoPress at 180°C and 250 bar. (6 min heating and pressing, 4 min cooling). The mounted samples were ground and polished using a Strues RotoPol-31/Roto-Force-4 and the polishing procedure described in Table 2-3.

Table 2-3: Grinding and polishing program for all samples

Step	Disc Name	grain size (µm)	force (N)	duration (min)
grinding	Piano 120	120	25	3
polishing	Allegro	9	20	5
polishing	Largo	3	15	8
polishing	DAC	1	15	8

Between each step, the specimens were thoroughly washed with water and with ultrasonic cleaning in isopropyl alcohol. After polishing the surface was inspected for free C and etched with Murakami to confirm eta-carbides.

2.3 C-content adjustment

If the metallurgy showed that the specimen is not in the two-phase region the C content of the hardmetal has to be adjusted accordingly. If the C content is too low, additional carbon black must be added to the powder sample. If the C content is too high, additional tungsten- and molybdenum-carbide powder needs to be added. Because of the small batch size of 150 g, weighting in multiple powders increases the probability of a methodical error. Therefore, it is preferable to increase the C content rather than trying to lower it.

To do so the stored powders are again, transferred into the milling drum and weighed. To raise the C activity small steps (~ 0.1- 0.3 wt%) of additional carbon black are preferred to avoid missing the two-phase region. After the addition of carbon black, the powder samples were treated as described in 2.2.

2.3.1 Sampling

To speed up the doping process, only small samples were taken for the 3rd and 4th batch and not the entire powder slurry was prepared. For this purpose, the grinding bowls were opened, the supernatant was removed and about 7-10 g of the powder was taken with the help of a laboratory spoon. To avoid losses, the spoon was rinsed back into the beaker with the supernatant. The small amount of powder slurry was dried at 70°C for 20 min. The dried sample was then prepared as described in 2.2. The advantage of this procedure is that in case the C content was not in the correct range, it is only necessary to open the grinding cup and add the required powder.

2.4 Characterisation

2.4.1 Density

Routinely, all samples were analysed for density using Archimedes' principle. Each sample was first weighed dry and then three times immersed in distilled water. Between each measurement, the sample was thoroughly dried with paper towels. To accurately determine the density of the liquid, the temperature was measured before and after with an alcohol thermometer. The density of the water was then taken from the table [22] according to the measured temperature. The density of the sample can be calculated with the following equation:

$$\rho_{sample} = \frac{(m_{dry} * \rho_{water})}{(m_{dry} - m_{immersed})} \qquad \text{Equation 2-1}$$

ϱ.....density ($g \cdot mm^{-3}$)

m_{dry}.....mass of the dry specimen (g)

$m_{immersed}$ .....mass of the specimen immersed in the water (g)

2.4.2 Hardness and fracture toughness

The hardness of the sample was tested with the method of Vickers Hardness (HV30). The indentations (5 per specimen) were done with an Emco-test M4U-025 and were evaluated on the LOM (Olympus GX51) which has the option to measure the length of the diagonals digitally:

$$HV = 1.854 \cdot \frac{F}{d^2} \qquad \text{Equation 2-2}$$

HV .....Vickers hardness (kg/mm²)

F .....load (kg force)

d.....arithmetic mean of the two diagonals (mm)

The fracture toughness was evaluated according to the method of Palmqvist-Shetty (Equ. 2-3), by measuring the crack length of the indentations with the LOM.

$$K_{Ic} = 0.0028 \cdot \sqrt{HV} \cdot \sqrt{F/L} \qquad \text{Equation 2-3}$$

K_{Ic} .....plane strain fracture toughness (MPa·m$^{1/2}$)

F .....load (kg)

L .....total crack length (mm)

2.4.3 Differential thermal analysis

For the investigation of the liquid phase formation temperature of the samples, differential thermal analysis (DTA) was employed. Each powder sample was prepared to specimens of ~440 mg and pressed with 155 MPa for 20 s. The analysis was conducted in a Linseis PT STA 1750 with an Al_2O_3 crucible and two heating cycles up to 1500°C in a purified 99.999 vol% Ar atmosphere. The temperature was calibrated with the [M_6C|WC|Co_{fcc}|Co_{liquid}] (1368°C) and the [Free C|WC|Co_{fcc}|Co_{liquid}] (1320°C) equilibria. The onset temperatures were evaluated using the Linseis TA Evaluation software.

2.4.4 Dilatometry

The measurements were carried out using a Netzsch DIL 402C. The samples were handled and pressed as in 2.2.2. For the measurements, a constant heating rate of 10 K/min to 1480°C was used and then held for 1 h. The atmosphere was Ar with a low rate of 50 mL/min. Only one dimension change can be measured. For this work, the height of the cylindrical samples was measured.

2.4.5 Powder X-ray diffraction

In preparation for the powder X-ray diffraction (XRD), the unmounted halves of the hardmetal specimens were debarked to create a plain surface. The samples were then mounted in the steel carriers of the autosampler using modelling clay and were then levelled with a piece of window glass.

All XRD measurements were carried out in a Malvern PANalytical MPD Pro with $CuK_{\alpha1,2}$ in range of 20 – 120° 2θ, with a step size of 0.02° 2θ and a counting time of 70 s per step. The diffractograms were taken with both $CuK_{\alpha1}$ and $CuK_{\alpha2}$ to minimise the intensity loss of the primary beam.

2.4.6 Scanning electron microscopy

The images were taken on an FEI SEM Quanta 200 using a backscattered electron detector (BSE) with a voltage of 20 kV and a spot size of 3.0 in a high vacuum environment. These images were also used for the evaluation of the grain-size distribution with the linear intercept method using the software ImageJ.

3 RESULTS

3.1 System investigation

3.1.1 Liquid phase formation temperature

To get a general idea of the thermodynamics of the systems used in this thesis, phase diagrams of all cemented-carbide systems were calculated using the CALPHAD software Thermo-Calc™ (database TCFe9). Figure 3-1 is an example of the W5MoC-Ni system. The remaining diagrams can be found in appendix 7.1.

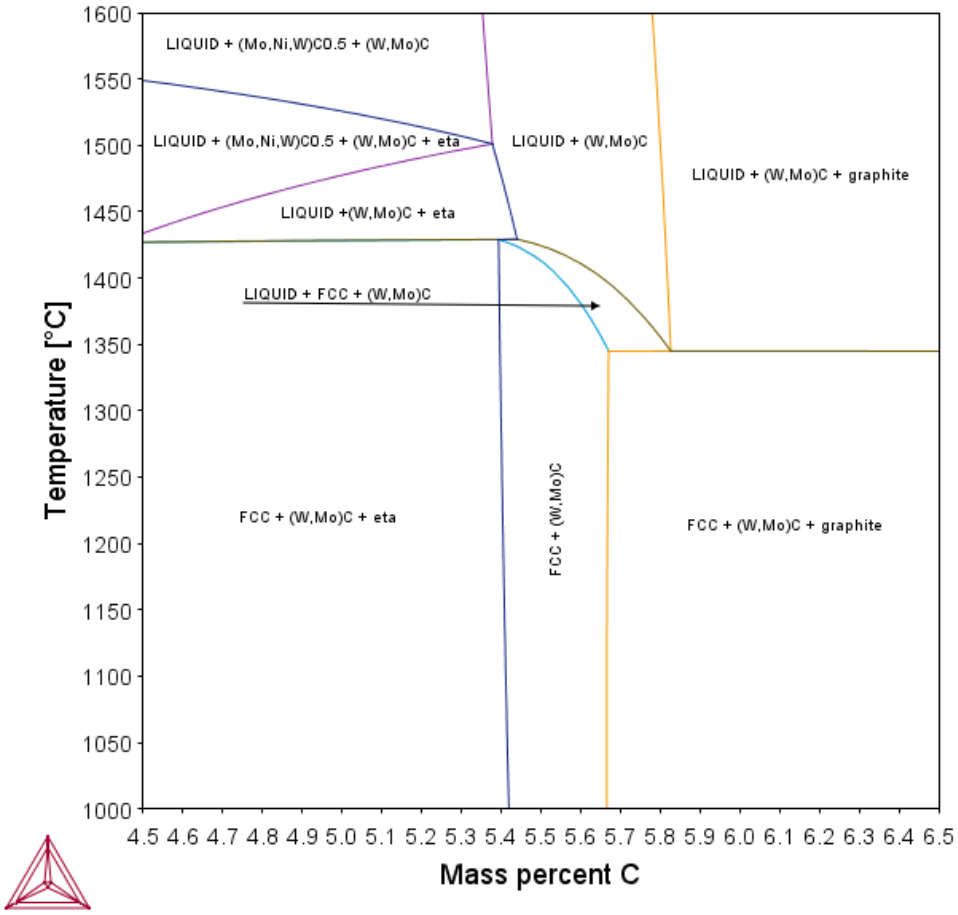

Figure 3-1: Calculated phase diagram of the $(W_{0.91}Mo_{0.09})C$ - Ni system

The most interesting pieces of information these diagrams provide is the range of the two-phase C window (FCC | (W,Mo)C region in Figure 3-1) and the liquid phase formation temperature (in short LPFT) of the binder as these can be compared with the results of the second heating cycle of the DTA. Table 3-1 shows the liquid phase formation evaluated with the DTA and Thermo-Calc™ for all samples. The temperatures for Thermo-Calc™ were measured via ImageJ directly from the phase diagrams.

Table 3-1: LPFT measured with DTA compared to the calculated temperatures

Sample	Onset ETA DTA (°C)	ETA CALPHAD (°C)	Diff (K)	Onset Free C DTA (°C)	Free C CALPHAD (°C)	Diff (K)
1A	1405.8	1429.7	23.9	1316.2	1345	28.8
1B	1358.4	1406	47.6	1298.7	1333.5	34.8
1C	1354.7	1406	51.3	1298.4	1333.5	35.1
1D	1401.6	1429.7	28.1	1314.7	1345	30.3
2A	1388.2	1408.5	20.3	1313.1	1315.8	2.7
2B	1349.4	1378.6	29.2	1326.4	1305.5	-20.9
2C	1348.1	1378.6	30.5	1324.7	1305.5	-19.2
2D	1390.7	1408.5	17.8	1315.7	1315.8	0.1
3A	1389.6	1392.3	2.7	1290.5	1324.8	34.3
3B	1346.9	1353.5	6.6	1271.6	1300.7	29.1
3C	1346.9	1353.5	6.6	1276.2	1300.7	24.5
3D	1388.4	1392.3	3.9	1290.9	1324.8	33.9
4A	1371.1	1371	-0.1	1288.5	1284.3	-4.2
4B	1337.9	1327.9	-10.0	1260.3	1255.8	-4.5
4C	1336.8	1327.9	-8.9	1262.6	1255.8	-6.8
4D	1370.9	1371	0.1	1288.3	1284.3	-4.0

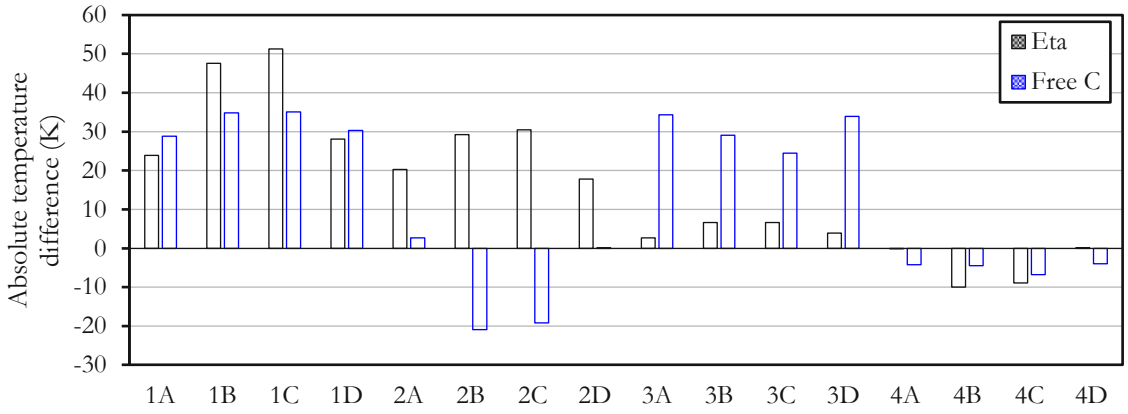

Figure 3-2: Absolute temperature difference between CALPHAD and DTA for eta and free C

Figure 3-2 shows how much the Thermo-Calc™ calculation deviates from the measured onset temperatures. Some trends can be derived from this diagram:

- For binder system 1 (Ni) the temperatures are calculated too high for both eta and free-C equilibrium.
- For binder 2 (Ni85Fe15), Thermo-Calc™ is in great accordance with the free-C LPFT of the W5MoC samples, but too low for the W15MoC samples. The eta-region LPFT temperatures are all too high.
- For binder 3 (NiCr), the LPFT in the eta range was predicted quite precisely, yet the free-C LPFT is too high.

- Binder 4 (Ni85Fe15Cr), was calculated very accurately with a maximum deviation of -10 K.

It can be assumed that the most crucial part for the accuracy of the calculations is the binder system since the difference between the pre-alloyed (hard-phase type A) and powder mixture (hard-phase type D) is neglectable and that the deviation for each hard phase is reproducible. Interestingly the most complicated binder system Ni85Fe15Cr was calculated with the highest accuracy for both sides of the C-window.

Zhang et al. [23] investigated the melting behaviour of (W,Mo)C-(Co,Ni) cemented-carbide systems with CALPHAT using the experimental data of the quaternary C-Mo-Ni-W system of Schubert et al. [19]. These systems had a fixed amount of 60 at% Ni. A comparison of their work with the results of this work can be seen in Figure 3-3 (9 at% Mo) and Figure 3-4 (24 at% Mo).

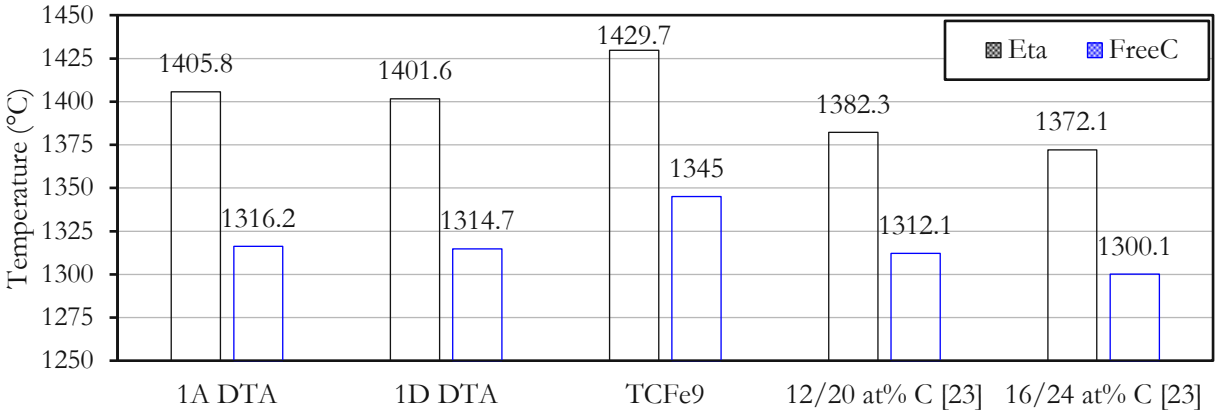

Figure 3-3: Comparison of the DTA and Thermo-Calc™ results of the ($W_{0.91}Mo_{0.09}C$)-Ni system with the results of Zhang et al. [23]

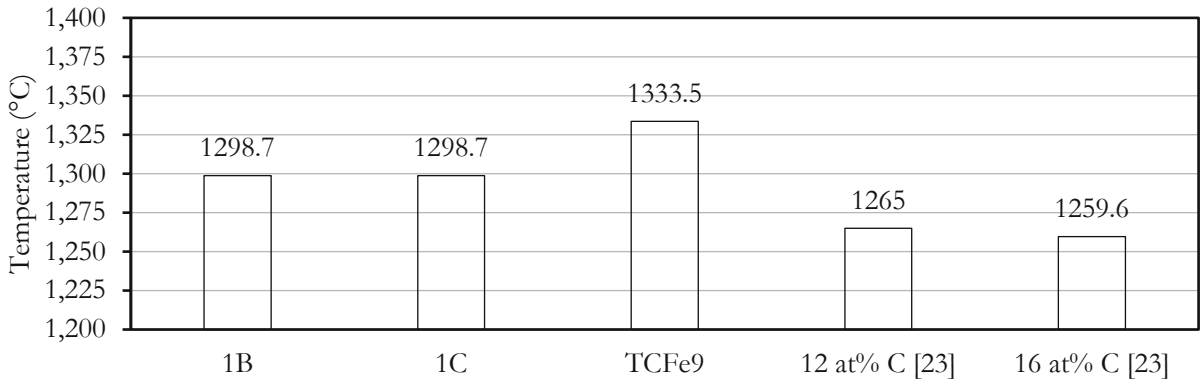

Figure 3-4: Comparison of the DTA and Thermo-Calc™ results of the ($W_{0.76}Mo_{0.24}C$)-Ni system with the results of Zhang et al. [23]

This comparison shows that the results of Zhang et al. deviate similarly to the Thermo-Calc calculations carried out in this work. The deviations are strongly dependent on which side of the two-phase region is considered. In general, for the comparable systems, the calculations of Zhang et al. predict the LPFT 20 – 30°C too low. However, for low Mo and high C content systems, the calculation was much more accurate.

In conclusion, the calculated LPFT deviate substantially from the measured temperatures the higher the concentration of Mo is in the (W,Mo)C solid solution, which is in accordance with the results of Zhang and his colleagues [23]. This may be due to the inappropriately described thermodynamics of the compound (W,Mo)C but also due to the inhomogeneity of the hard-phase grains which develops upon sintering [12] (see chapters 3.1.2, page 16 and 3.2.2, page 20) and does not reflect thermodynamic equilibrium. Hence, calculations of phase equilibria must be seen with certain precaution when applied to predict the sintering behaviour of (W,Mo)C hardmetals.

3.1.2 Powder XRD

The diffractograms of the samples were put together in combined diagrams, to compare the hard phases and the binder systems which are displayed in appendix 7.2. All diffractograms were refined with a default Rietveld fit, provided by the software HighScore™. A list of the assigned reflections for the diffractogram shown below can be found in Table 3-2.

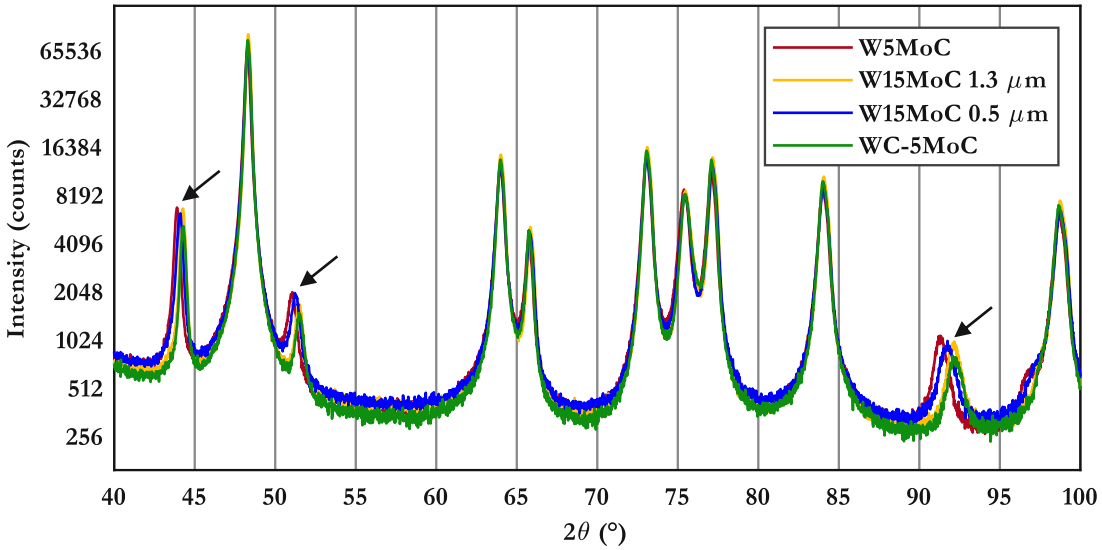

Figure 3-5: Comparison of the different hard phases for binder 1 (Ni) from 40° to 100° 2θ

Figure 3-5 shows the combined diffractograms of all samples with binder 1 from 40° to 100° 2θ because in this range the relevant binder reflections are more visible. The hard-phase reflections overlap precisely while the visible reflections for the binder (marked reflections at 44°, 51° and 92° 2θ) show some deviation between the different hard phases. The remaining diffractograms are displayed in appendix 7.2.

Table 3-2: Result for the Rietveld refinement for sample 1A in the range of 40° to 100° 2θ

Reflection Nr.	Pos. 2θ	assigned Phase	h	k	l	multiplicity
3	43.8	Ni (binder)	1	1	1	8
4	48.2	(W,Mo)C	1	0	1	12
5	51.1	Ni (binder)	0	2	0	6
6	63.9	(W,Mo)C	1	1	0	6
7	65.7	(W,Mo)C	0	0	2	2
8	73.0	(W,Mo)C	1	1	1	12
9	75.1	Ni (binder)	0	2	2	12
10	75.4	(W,Mo)C	2	0	0	6
11	77.0	(W,Mo)C	1	0	2	12
12	83.9	(W,Mo)C	2	0	1	12
13	91.2	Ni (binder)	1	3	1	24
14	96.6	Ni (binder)	2	2	2	8

3.1.2.1 Investigation of the hard phase

The diffractogram in Figure 3-5 and appendix 7.2 show the following problems regarding the hard-phase reflections: Firstly, there is no noticeable shift between the cemented-carbide specimens with 9 at% Mo and 24 at% Mo and secondly, the splitting of the $CuK_{\alpha1}$ and $CuK_{\alpha2}$ reflections is missing.

Depending on the Mo content the c-lattice parameter of the solid solution (W,Mo)C changes slightly from 2.8367 Å (pure WC) to 2.8346 Å for $(W_{0.91}Mo_{0.09})C$ and 2.8305 Å for $(W_{0.76}Mo_{0.24})C$, which was proven by Schuster et al. [8] (Figure 1-2, page 4). This results in a slight shift of the reflections for Miller indices $l > 0$ and can be seen especially good for the 002 lattice plane [8]. To get accurate values for these expected shifts a PowerCell™ calculation of the diffractograms was conducted. The result is displayed in Table 3-3. However, these shifts for the mentioned reflections are not noticeable in the diffractograms of the sintered cemented carbides.

Table 3-3: Result of the PowerCell™ calculations for the hkl 002 reflections and the corresponding 2θ value

Phase	h	k	l	2θ (°)	d/Å
WC	0	0	2	65.787	1.41835
$(W_{0.91}Mo_{0.09})C$	0	0	2	65.842	1.41730
$(W_{0.76}Mo_{0.24})C$	0	0	2	65.950	1.41525

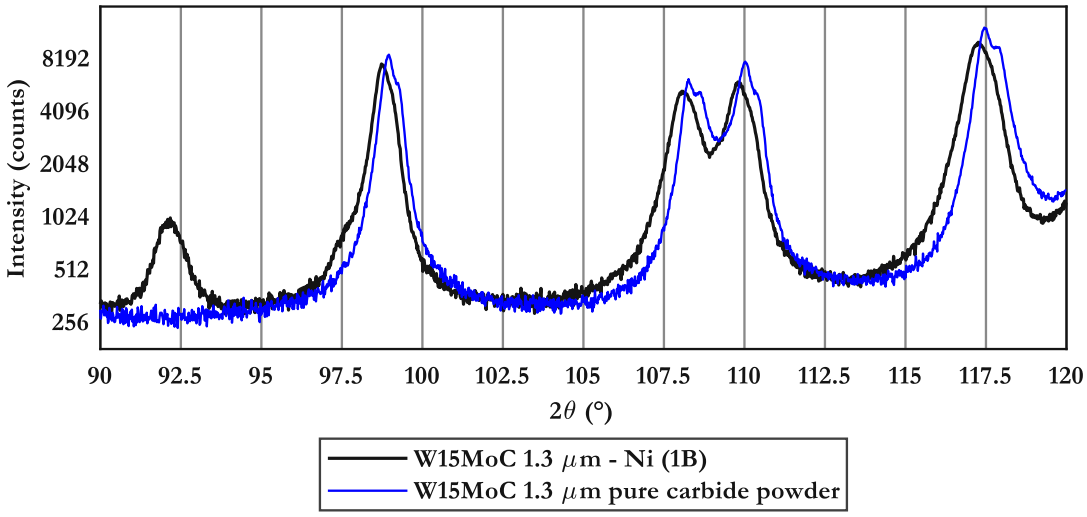

Figure 3-6: Comparison of the cemented carbide 1B with the pure hard phase W15MoC at high 2θ to emphasise the shift

Figure 3-6 shows a comparison of the measured diffractograms between pure hard powder (blue) and a hard metal sample 1B (black). The diffractogram starts at 90° 2θ to make the details more visible. The splitting of $CuK_{\alpha1}$ and $CuK_{\alpha2}$ is pronounced for the pure powder, while for the sintered cemented carbide the shoulder disappears. This means that the broadening of the reflections of the hard phase is a result of the sintering process. This covers the shifts of the different hard phases and the splitting of the two primary beams.

This broadening is likely due to the "core-rim"- like the structure of individual grains seen in the SEM images (Figure 3-11, page 21) and in the results of Schwarz et al. [12]. This raises the question of why this core structure is not shown in the XRD. A possible answer could be, that the CuKα X-rays cannot reach the core with the increased Mo content.

The Attenuation of X-rays in a solid material is dependent on the mass attenuation coefficient (MAC) of the material and is described by the Beer-Lambert law (Equ. 3-1). The MAC of (W,Mo)C is calculated with Equ 3-2 [24].

$$I = I_0 \cdot e^{-\mu t}$$ Equation 3-1

$$MAC_{(W,Mo)C} = x_W \left(\frac{\mu}{\rho}\right)_W + x_{Mo} \left(\frac{\mu}{\rho}\right)_{Mo} + x_C \left(\frac{\mu}{\rho}\right)_C$$ Equation 3-2

I .....Intensity of the beam

x_i .....Molar fraction

μ.....Attenuation coefficient (cm^{-1})

ϱ.....Density (g/cm^3)

t.....Layer thickness (cm)

Table 3-4: MAC for CuKα (λ = 1.5406 Å) for each element of Equ. 3-2.

Element	(μ/ϱ) (cm^2/g) [25]
W	$1.705 \cdot 10^2$
Mo	$1.565 \cdot 10^2$
C	4.576

Table 3-5: MAC for CuKα (λ = 1.5406 Å) for each hard phase composition

Hard phase	MAC μ/ϱ (cm^2/g)	ϱ (g/cm^3)	μ (1/cm)
$(W_{0.91}Mo_{0.09})C$	86.91	15.13	1314.92
$(W_{0.76}Mo_{0.24})C$	85.86	14.05	1206.30

For the layer thickness of the core-rim structure, a single grain from sample 3A was used to simulate the beam path (Figure 3-7) and measured with the software ImageJ. Unfortunately, it is impossible to measure the Mo concentration of the individual layers and therefore, the attenuation coefficient of the layers was defined as such: μ[rim] ≈ μ[$(W_{0.91}Mo_{0.09})C$], μ[core] ≈ μ[$(W_{0.76}Mo_{0.24})C$]

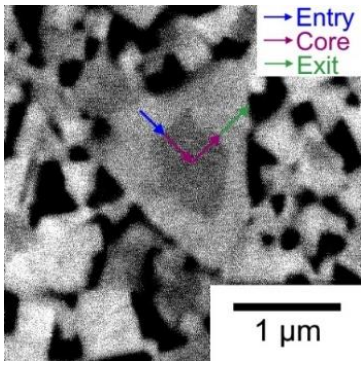

Figure 3-7: Simulated beam path inside a grain with core-rim structure

The result of this thought experiment (Table 3-6) is that due to the high attenuation only a fraction of the radiation (15% of the initial radiation for the selected grain) of the inner core reached the detector. Besides the fact that the exact composition of the inner "phase" is unknown, the following simplifications were made: The Beer-Lambert law is designed for transmission, which was assumed in this case for the diffraction in a first approximation. Secondly, the selected grain is very large (~2 μm) in relation to the average (d90[3A]= 0.65 μm, Figure 3-17, page 26) and the contrast of the SEM-BSE image recording suggests a phase boundary that

probably does not exist. It is therefore reasonable to assume a continuous change in concentration, especially given the large number of very fine grains in the microstructure.

If this "core" phase had defined lattice parameters, it should be possible to recognise it by a shoulder on the hard-material phase peaks. Due to the high electron density of tungsten, the intensity of the hard-material peaks is very high. As I was able to show, much of the intensity of the beam is lost even at shallow penetration depths. Thus, a shoulder would be easily swallowed especially with the broadening effect of the sintered sample. This presumably means that the peaks are broadened due to the Mo segregation within the grains, which leads to stray lattice distortion which then leads to less precise diffractograms.

Table 3-6: Result of the attenuation of the beam path shown in Figure 3-7

Path	Angle (°)	Length (µm)	L (cm)	I/I_0
Entry	-45	0.361	$3.6 \cdot 10^{-4}$	0.62
Core 1	-45	0.417	$4.2 \cdot 10^{-4}$	0.38
Core 2	45	0.32	$3.2 \cdot 10^{-4}$	0.26
Exit	45	0.392	$3.9 \cdot 10^{-4}$	0.15

3.1.2.2 XRD investigation of the binder

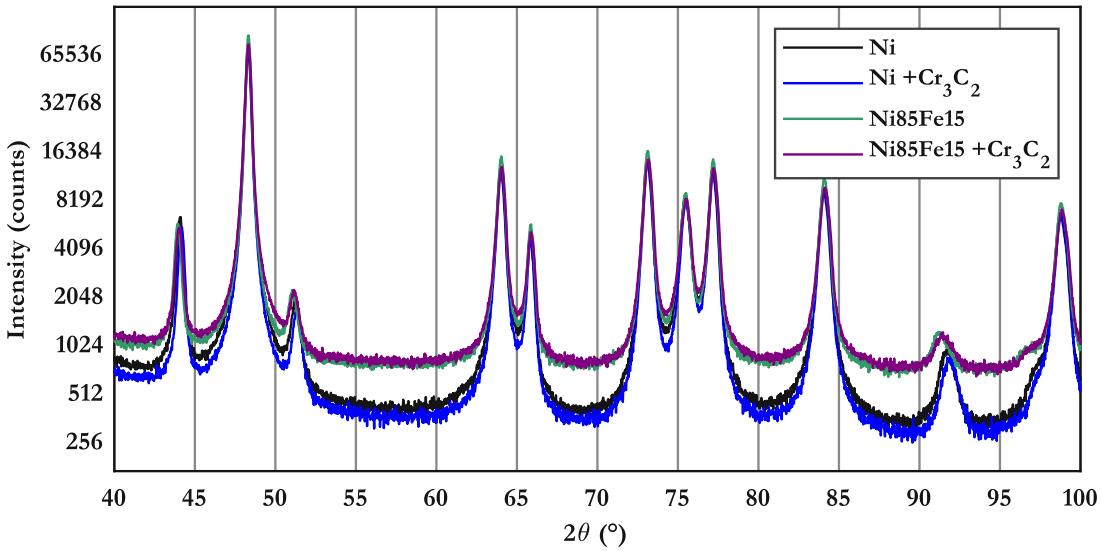

Figure 3-8: Comparison of the different binder phases for hard-phase type C (W15MoC 0.5 µm)

Figure 3-8 shows that the diffractograms of the same hard phase (ultra-fine type C) do not contain the same shifts as seen in Figure 3-5. This means that the shifts for reflections 44°, 51° and 92° 2θ can probably be attributed to the different W and Mo content dissolved in the binder depending on the different hard-phase types. An attempt was made to investigate the W content in the binder with the help of model alloys. However, it was not possible to make quantitative conclusions, as the data available was too limited. Furthermore, the binder lattice parameter determination of the Rietveld analysis was not accurate enough, presumably due to the broadening of the hard-phase peaks discussed in the previous chapter (3.1.2.1, page 16).

3.2 Metallurgy and sintering behaviour

3.2.1 Porosity

The initial aim was to adapt the sintering conditions to this new type of cemented carbides. The starting point was the implementation from Schwarz et al. [11, 12]. The first sintering tests resulted in samples with eta-carbides (low C content) in the microstructure and residual porosity. The first goal was therefore to lower the porosity upon vacuum sintering.

The samples of the hard-material type B (W15MoC 1.3 µm) showed increased porosity compared to the other hard phases. The first sintering tests were carried out at 1440°C, as this is the typical sintering temperature for WC-Co cemented carbides. To lower the porosity, the sintering temperature was first gradually increased to 1480°C, a common temperature for Ni-binder cemented carbides [26]. This was then maintained for all subsequent sintering runs. Figure 3-9 shows a comparison of the first 3 sintering tests. The porosity for each sample is a) 2.84% b) 3.34% c) 2.53%, respectively (evaluated with the software ImageJ), which is not an improvement. Thus, the increased temperature did not improve the microstructure for Type B samples but did so for the other hard-phase grades.

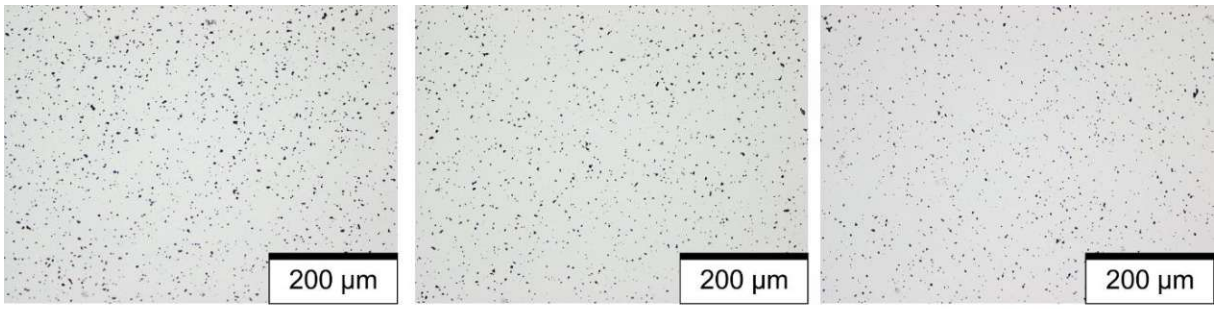

Figure 3-9: Comparison of the microstructure of hard-phase type B at different sintering temperatures

The next attempt at reducing the residual porosity was to increase the milling time. After the addition of carbon black to increase the C content, the powder samples were milled again to ensure homogeneity. This extra milling time diminished the residual porosity for hard-phase type A. For B, C and D an additional milling step of 72 h compared to A were conducted. Since every milling step with fresh cyclohexane reduces the C content approx. by 0.1 wt%, extra carbon black was added to compensate for this long milling time. The added amount of 0.375 wt% was too much which resulted in free C in the microstructure. After the reduction of the C activity, which took another 47 h of milling, all samples of batch 1 (Ni binder with no grain-growth inhibitors) had 0.01-0.02% residual porosity. This almost perfect result could not be reproduced for hard-phase type B in the following experiments.

Table 3-7 and Figure 3-10 show the results for the residual porosity for all final samples of all batches and the individual milling times. The difference in the milling times is the result of the C-content adjustment. The significant difference between hard-phase type B and the rest is quite noticeable. It was not possible to find a reason for the behaviour of sample 1B. The total milling time is not an explanation since all specimens of hard-phase type B have similar total milling times. 1B is the only of the four B-based samples that landed in the free-C equilibrium during C-content adjustment. Therefore, a plausible explanation is that milling in high-C activity (above the two-phase region) causes an unknown reaction that increases the sintering activity of the pre-alloyed powder. To confirm this hypothesis, it would be necessary to intentionally increase the C content of the later batches into the free-C equilibrium and reduce it again. Since C content correction is a time-consuming procedure, this was not tested for the remaining B-based specimens in the scope of this thesis.

Another unique feature of sample 1B is that the binder is pure Ni. An alternative explanation is that for the samples of batches 2 to 4, the additional alloying elements of the binder further reduce the sintering activity.

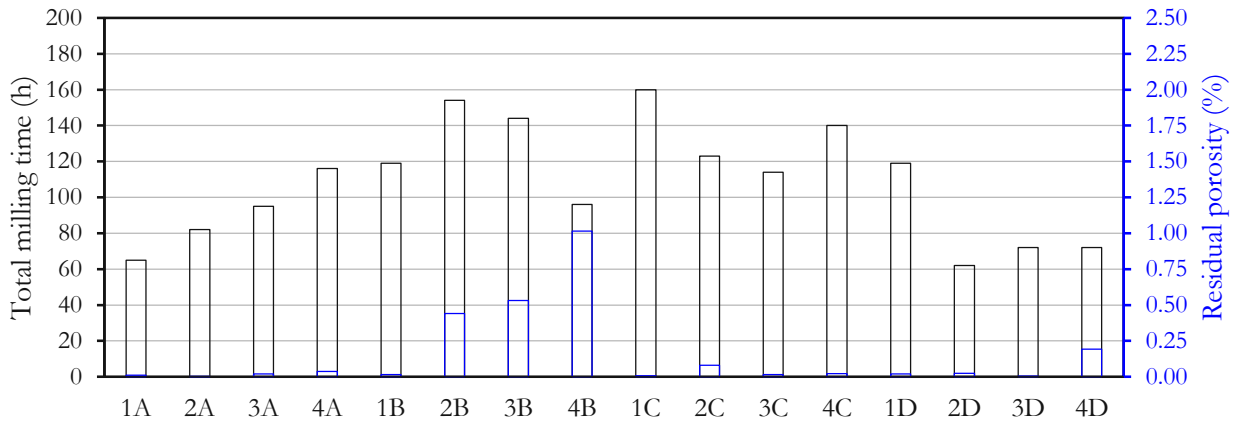

Figure 3-10: Graphic comparison of the residual porosity and total milling time

Table 3-7: Residual porosity and total milling time of all the final samples

Symbol	Sample	Residual porosity (%)	Norm class	Total Milling Time (h)
1A	W5MoC -Ni	0.01	A02	65
1B	W15MoC 1.3 -Ni	0.02	A02	119
1C	W15MoC 0.5 -Ni	0.01	A02	160
1D	WC-5MoC -Ni	0.02	A02	119
2A	W5MoC -NiFe	0.00	A02	82
2B	W15MoC 1.3 -NiFe	0.44	A06	154
2C	W15MoC 0.5 -NiFe	0.08	A04	123
2D	WC-5MoC -NiFe	0.02	A02	62
3A	W5MoC -NiCr	0.02	A02	95
3B	W15MoC 1.3 -NiCr	0.53	A06	144
3C	W15MoC 0.5 -NiCr	0.02	A02	114
3D	WC-5MoC -NiCr	0.00	A02	72
4A	W5MoC -NiFeCr	0.04	A02	116
4B	W15MoC 1.3 -NiFeCr	1.02	A08	96
4C	W15MoC 0.5 -NiFeCr	0.02	A02	140
4D	WC-5MoC -NiFeCr	0.19	A04	72

3.2.2 LOM and SEM images

The figures on pages 21 -24 show a comparison of all the final specimens of each hard phase as LOM and SEM images. The LOM images have a magnification of 200x. The SEM images were taken with a magnification of 10,000x. All these samples are vacuum sintered at 1480°C with 100 mbar Ar atmosphere and have a two-phase microstructure, which was confirmed by etching with Murakami.

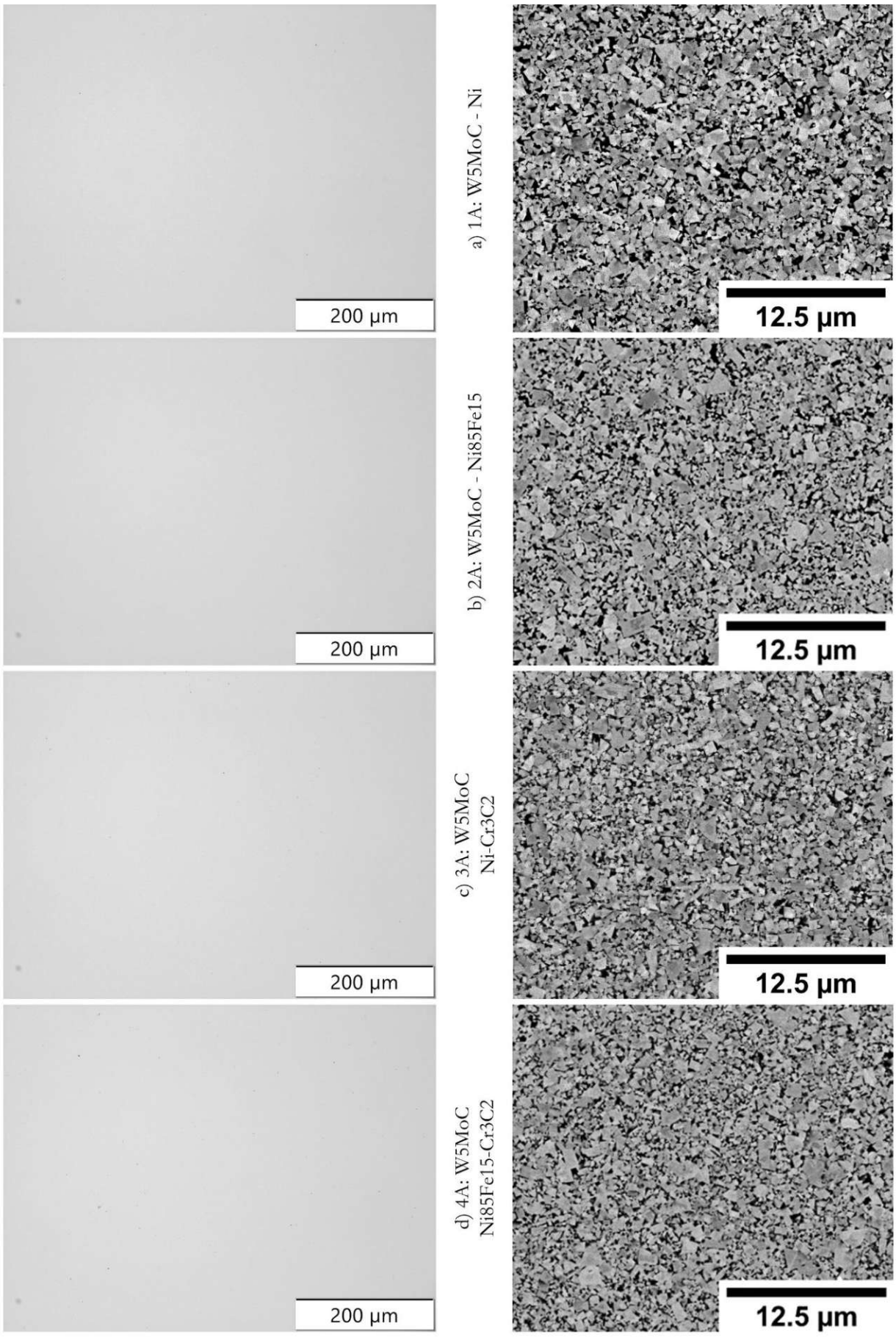

Figure 3-11: Microstructure of the final hard-phase type A specimens

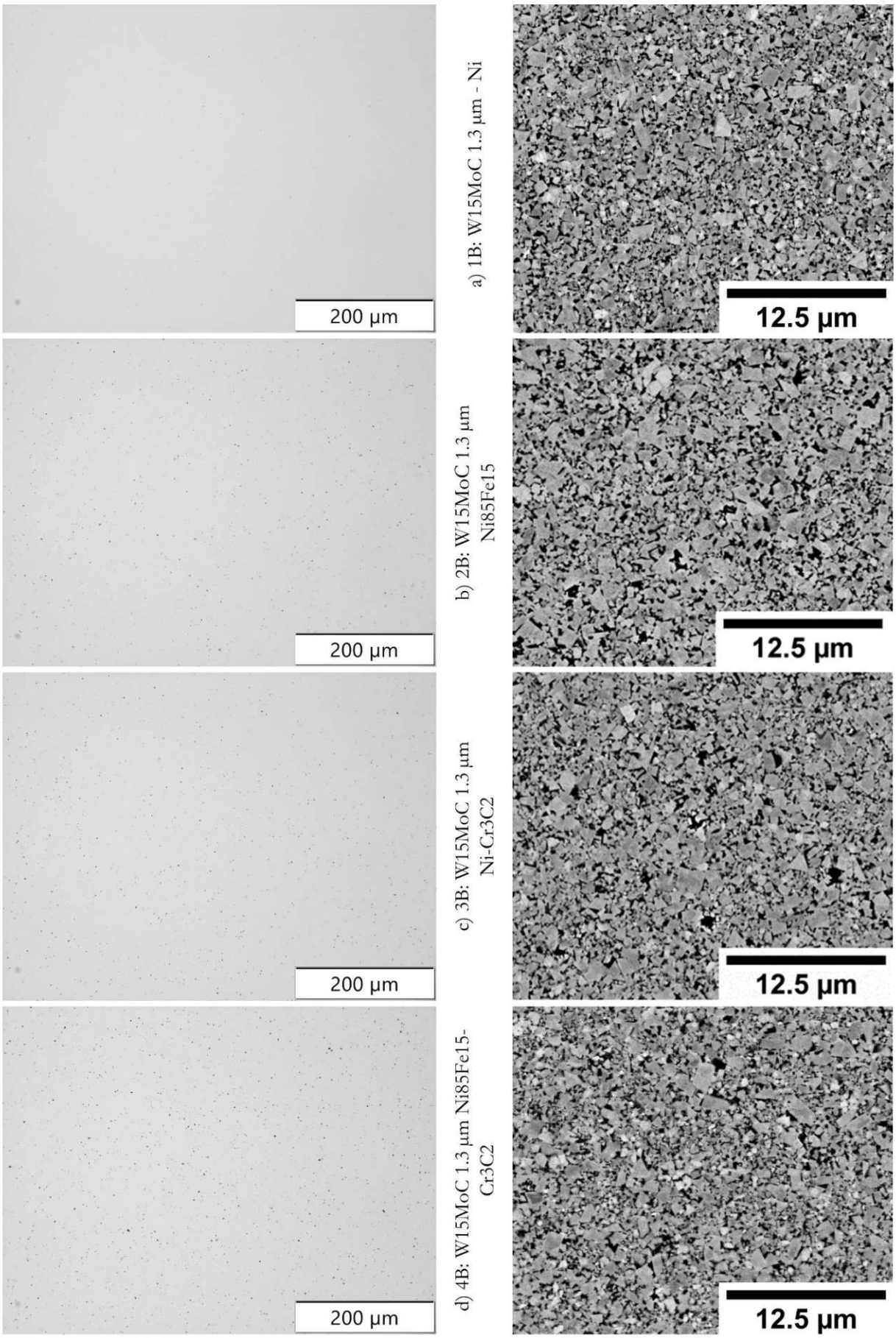

Figure 3-12: Microstructure of the final hard-phase type B specimens

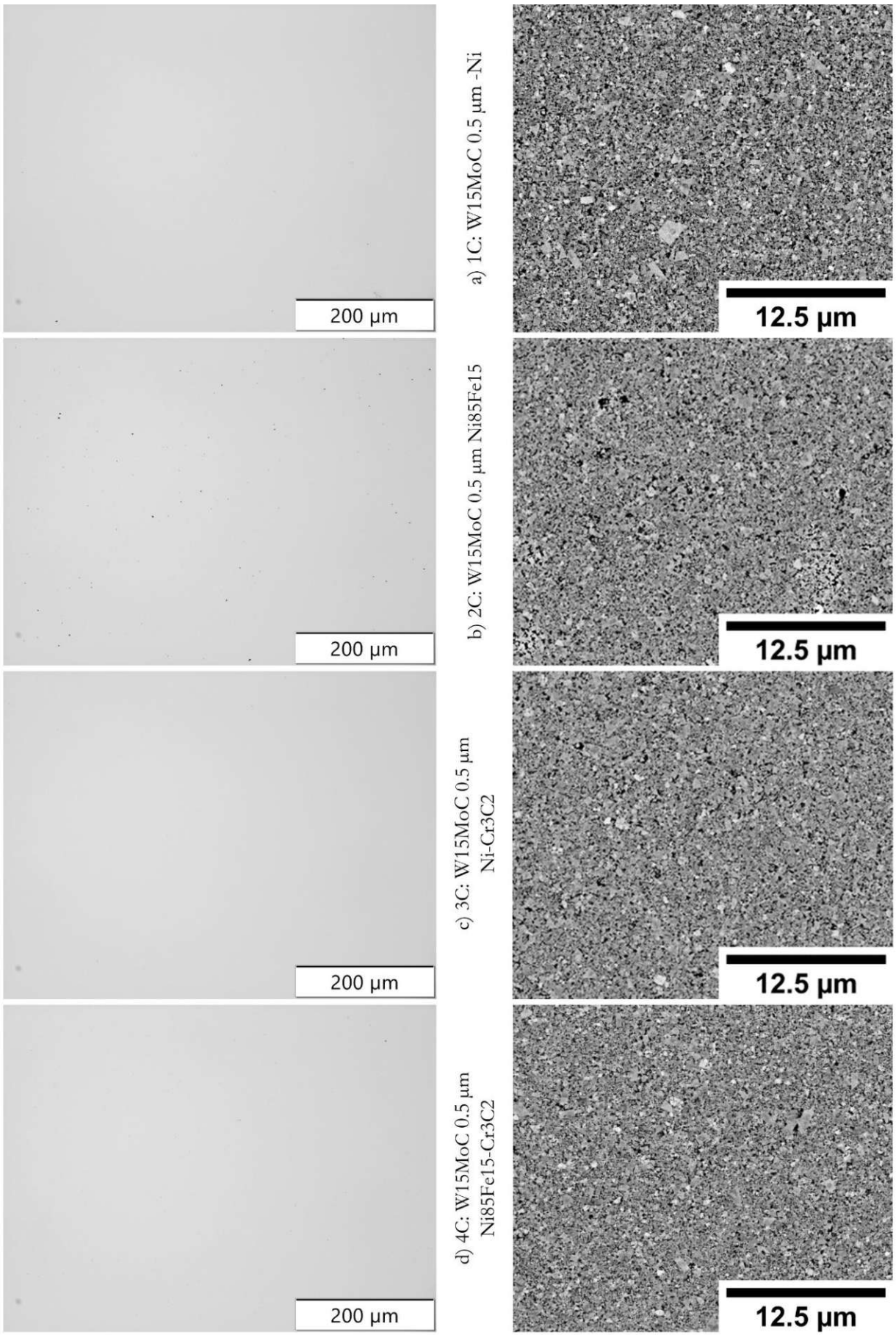

Figure 3-13: Microstructure of the final hard-phase type C specimens

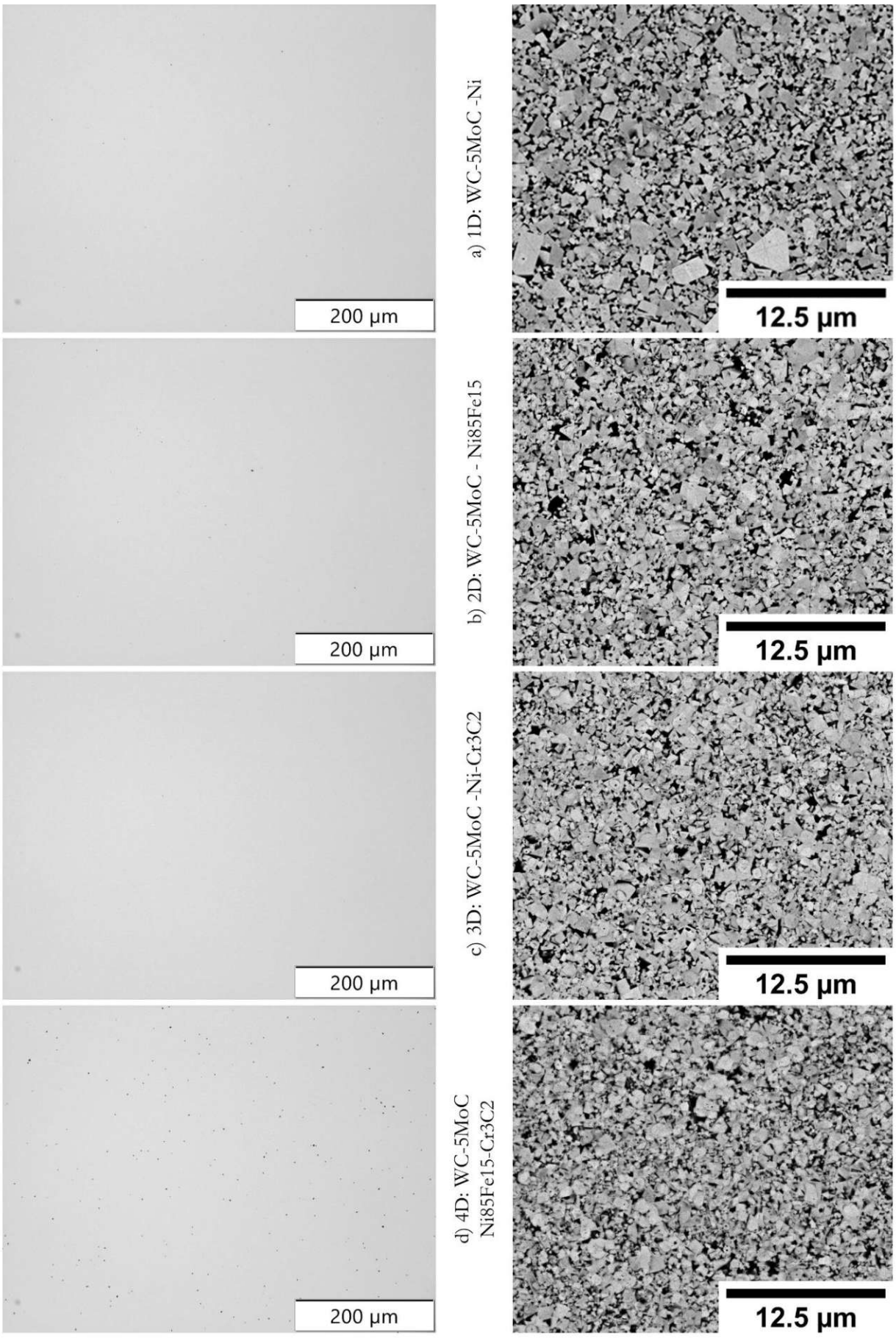

Figure 3-14: Microstructure of the final hard-phase type D specimens

Figure 3-11 to Figure 3-14 show that it was possible to create hardmetal specimens of good quality in vacuum conditions. As discussed in 3.2.1(page 19) samples of hard-phase type B (Figure 3-12, page 22) have some residual porosity. Examining the SEM images, a noticeable effect of the Mo addition is the presence of rounded edges of the individual grains, as also noted for the Co-binder samples [11-14]. Another phenomenon similar to (W,Mo)C-Co hardmetals is that some grains show a darker centre (e.g. Figure 3-11c SEM, centre) similar to the microstructure in [11, 12]. The SEM images were taken with a BSE detector which means that a dark spot means lower atomic weight. In this case, this suggests a higher concentration of Mo in the centre of the individual grains, resulting in a core-rim structure like the microstructure of cermets [1] but different from observations by Liu et al. [10], as their (W,Mo)C ceramics had a W-rich core. A reason for this could be the increased solubility of Mo in the liquid binder as described by Akmoran et al. [20], resulting in the W rich reprecipitations in the rim of the grains. This inhomogeneity cannot resolve in the given sintering time and temperatures, resulting in this core-rim structure. This also explains the already discussed broadened reflections in the XRD diffractograms (3.1.2.1, page 16).

Such core-rim grains are not visible for specimens made with the powder mixture of WC and Mo_2C (type D, Figure 3-14). Type-D cemented carbides show 2 unique properties which differentiate them from the pre-alloyed samples: the SEM images of the specimens show small black spots inside the individual grains them and the addition of Cr_3C_2 results in an increase of the rounded edges. These dark spots could be residual Mo_2C or free C from a decomposition reaction of the solid solutions, similar to the microstructural observations by Liu et al. [10], yet less pronounced.

3.2.3 Grain-size distribution

Grain-size distribution was evaluated using the linear-intercept method and was categorised as shown in Figure 3-15 and Figure 3-16. For hard-phase samples of types A, B and D, 15 categories from 0 to 2.0 µm were used. The ultra-fine hard-phase type C had to be categorized in a smaller range from 0 to 1.2 µm. Figure 3-15 and Figure 3-16 are an example of a comparison of the grain size of samples without (left) and with Cr_3C_2 addition (right). The remaining comparisons are displayed in appendix 7.3.

Cr_3C_2 was added as a grain-growth inhibitor, which usually has the effect of narrowing the grain-size distribution. [1, 26] Quantitative information of these grain-size distributions can be extracted using the d10, d50 and d90 values, e. g. d90 value represents the grain size in which 90% of the grains are contained. The smaller the value, the narrower the grain-size distribution.

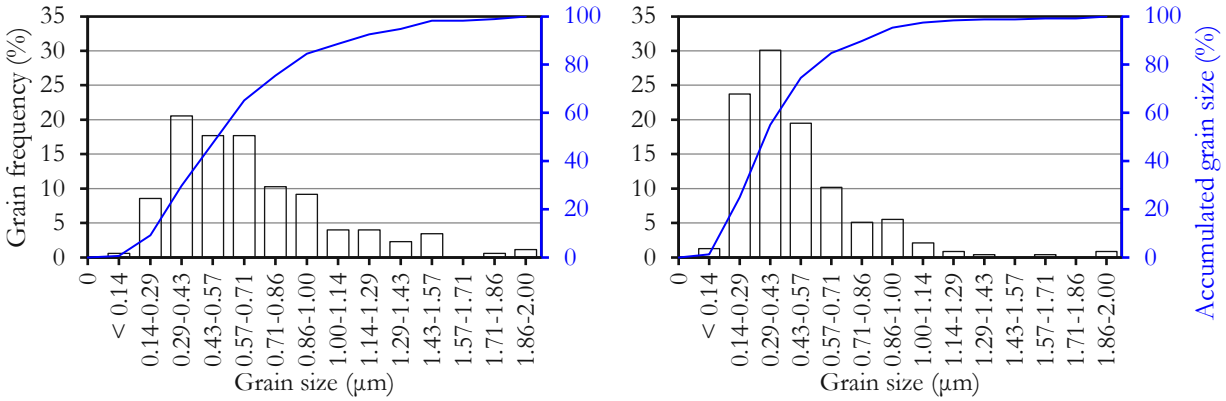

Figure 3-15: Comparison of the grain-size distribution of samples 2B (left) and 4B (right)

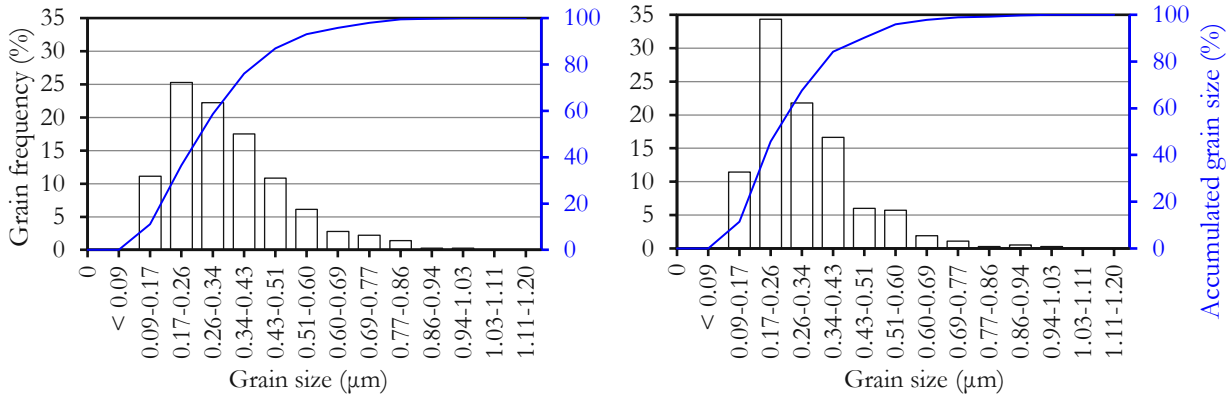

Figure 3-16: Comparison of the grain-size distribution of samples 2C (left) and 4C (right)

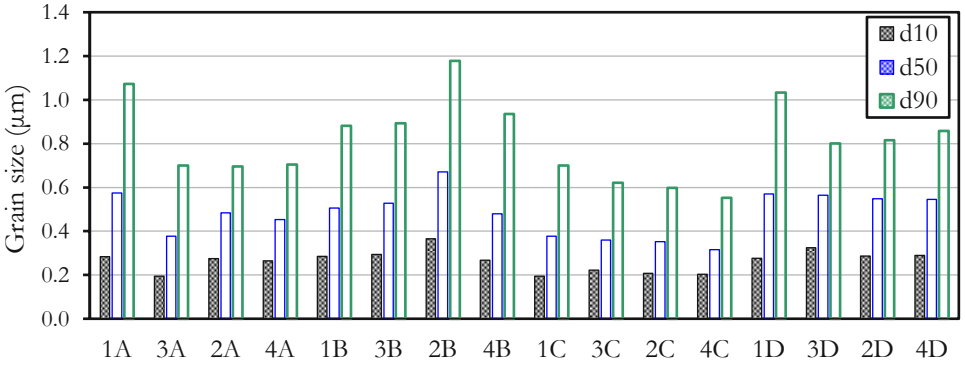

Figure 3-17: Comparison of d10, d50 and d90 values of all samples

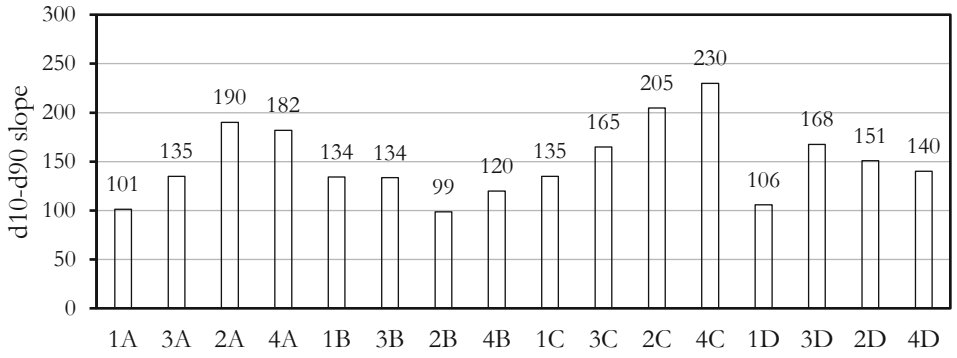

Figure 3-18: Comparison of the d10-d90 slope of all samples

Figure 3-17 shows a comparison of the d10, d50 and d90 values for all samples and Figure 3-18 shows the corresponding slopes. The samples are sorted by hard-phase type while putting the pure binder and the samples with Cr_2C_3 addition side-by-side for easier comparison. The slopes provide information on how narrow the grain-size distribution is. The steeper, the more uniform and better it is. Looking at the results in Figure 3-18, the addition of the chromium to the binder did not improve the results for samples 1B compared to 3B, 2A to 4A and 2D to 4D, however, it did for the rest. For 1B, perhaps the blatant difference in sintering behaviour is responsible for the lack of significant improvement, as the microstructures of samples 1B and 3B are quite different (see Figure 3-12). For 2A and 2D, it seems that the specific composition of the binder alloy Ni85Fe15 with the 5 wt% Mo content results that the addition of another alloying element promoting grain growth instead of inhibiting it. Perhaps a different carbide former could lead to a better result.

3.2.4 Sintering behaviour

3.2.4.1 Mass loss during sintering

As described in 2.2.2 all samples were weighed before and after the sintering process. The data for each hard phase and binder system was combined and is shown in Figure 3-19. The mass loss of the specimens of the ultra-fine type C (W15MoC 0.5 µm) is approximately twice as high as that of the hardmetals of type B and D. The difference cannot be defined more precisely because of the standard deviation. However, the difference is significant. A plausible explanation for this behaviour is certainly the difference in the specific surface area of the hard powders. The ultra-fine powder has a considerably larger surface area, and thus carries more oxygen and moisture into the sintering process, which leads to a greater C loss. This has a measurable effect on the mass loss, but can also be seen in the fact that the ultra-fine type C powders were very complex in the C-content adjustment.

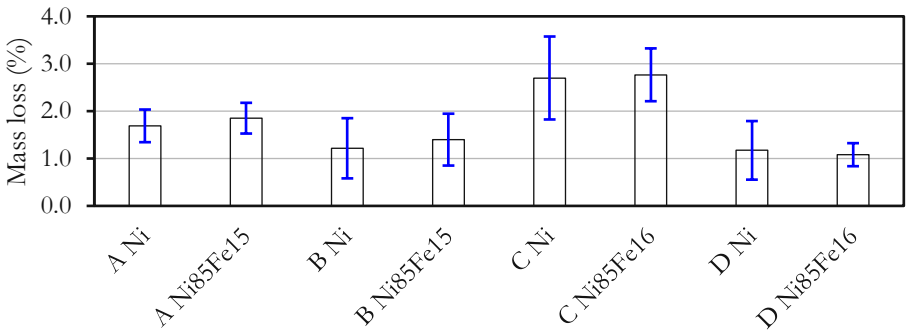

Figure 3-19: Comparison of the mass loss of each hard phase and binder system

3.2.4.2 Density

The samples were measured as described in 2.4.1. Figure 3-20 shows a comparison of the density of different sample systems. The replacement of W in the hard phase has a significant effect. Samples with the hard phase of type B and C have a 20% lower W content and therefore their density is reduced by ~ 1 g/cm³.

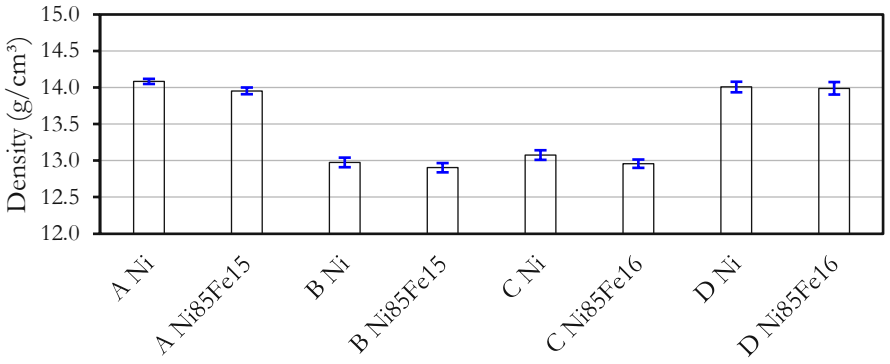

Figure 3-20: Density of all the sample systems

3.2.4.3 Total Shrinkage

Figure 3-21 shows the dimension of the cylindric specimens which were used to determine the total shrinkage of the individual specimen.

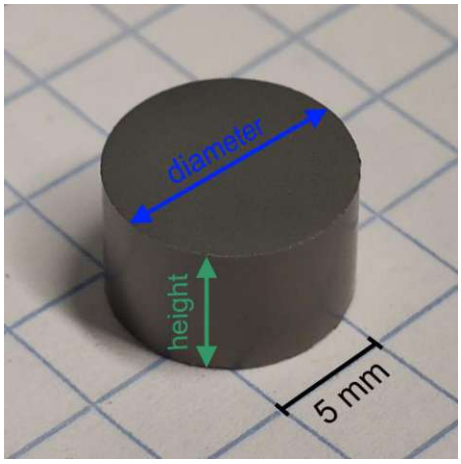

Figure 3-21: Example for a sintered sample and the measured dimensions

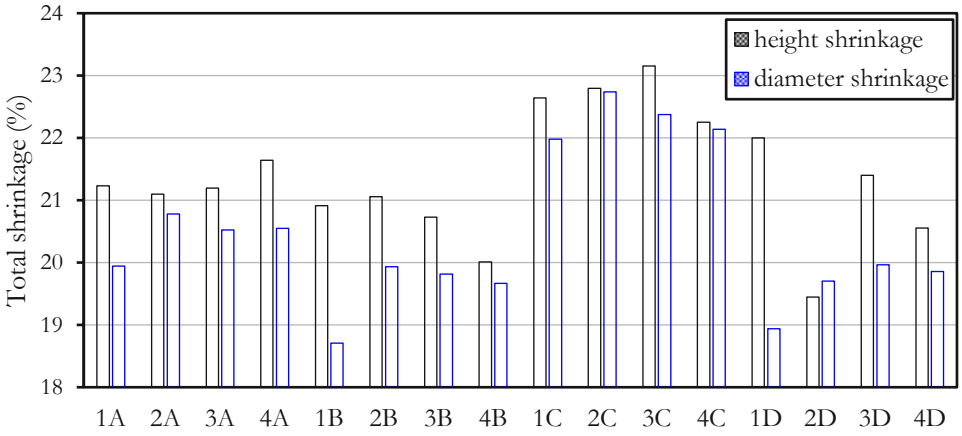

Figure 3-22: Dimensional loss of each cylindrical specimen

Figure 3-22 shows a comparison of the mean total shrinkage for each sample sorted by the hard-phase type. Like with the mass loss, type C is the hardmetal with the greatest total shrinkage but the difference to the other hard-phase powders is not as drastic as with the weight loss. An interesting trend is visible for binder system 1 (Ni): For these specimens, the difference between the shrinkage of the diameter and height is slightly greater than for the other binder systems.

3.2.4.4 Dilatometry

To further investigate how the new cemented-carbide systems behave during sintering dilatometry was conducted. After the C content of the samples had been set correctly the samples required for this were pressed and prepared in the same way as the sintered samples (see chapter 2.2.2). Unlike the sintered samples, the dilatometer samples were heated with a linear profile, i.e. the plateau at 1250°C was skipped. This shortened the measurement time, ensured linearity and makes this method comparable with the differential thermal analysis (DTA). Figure 3-23 is an example of such a comparison of the methods. The blue line is the measured shrinkage of the height which is in great accordance with the measured height shrinkage of the sintered samples (Figure 3-22, 21% for 1B). In Figure 3-23, the green line represents the shrinking rate (time derivative dL/dt). This line illustrates the changes in shrinkage rate more clearly than the blue line and therefore holds most of the information concerning the reactions taking place at a given temperature. For cemented carbides, most of the shrinkage occurs before the liquid-phase formation (LPF) of the binder [1, 3, 16], which is represented by

the first large peak of the green curve starting at ~1175°C (Figure 3-23, A). Above 1350°C is the point where the LPF starts, which is sometimes noticeable by another sharp drop of the shrinkage rate curve (Figure 3-23, B). [3]

The LPFT during sintering was also investigated in the DTA and is dependent on the C content of the specimen. In Figure 3-23, two DTA curves can be seen: The purple curve represents the [(W,Mo)C|Ni|η] equilibrium and the red curve represents the [(W,Mo)C|Ni|free C] equilibrium. These two equilibria are almost invariant and are therefore easier to define in the sample composition. As described in 2.4, page 10, the specimens for the DTA and the dilatometer were green body samples. Therefore, both the dilatometry and the first heating of the DTA can be understood as an approximate sintering process. The diagrams for all samples can be found in appendix 7.4.

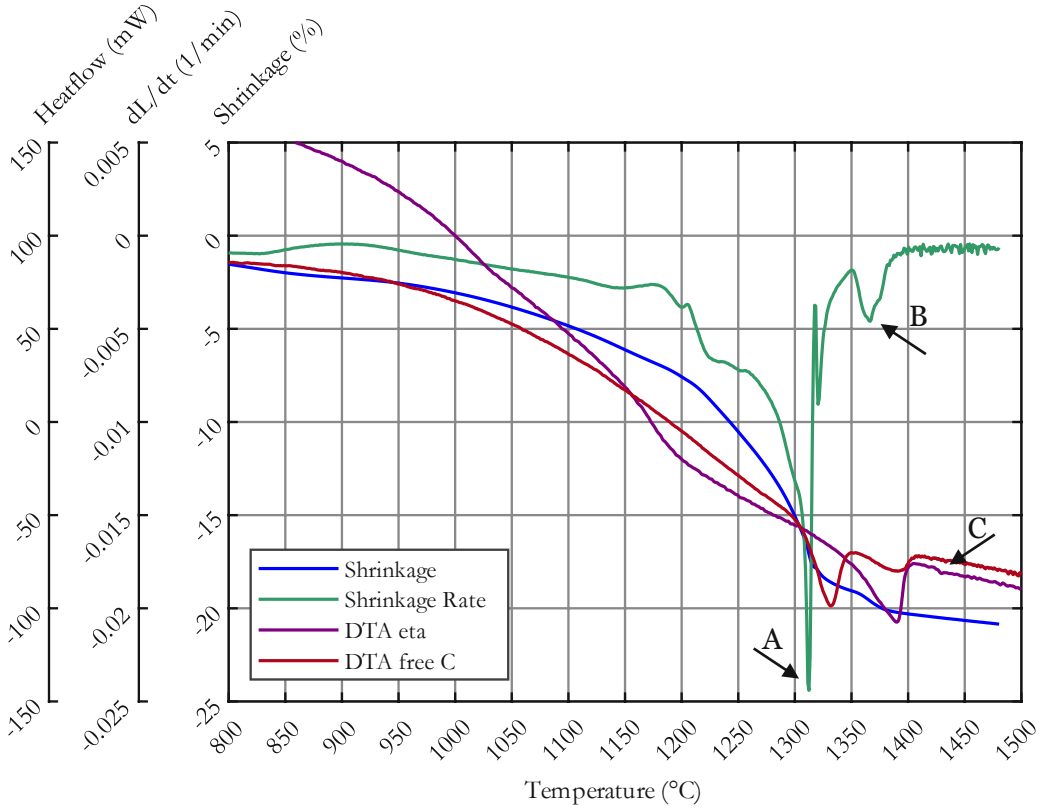

Figure 3-23: Combined diagram of dilatometer and DTA plotted against the temperature for sample 1B

To ensure that the C content of the dilatometer samples is the same as that of the sintered samples, a metallurgic examination of series 2 (Ni+Cr) was carried out. This showed that the C activity in the dilatometer is the same as that in the vacuum sintering furnace for hard-phase types, and therefore the sintering behaviour is comparable. However, a consistent investigation of cemented carbides on the dilatometer is very difficult, as the sintering behaviour is strongly influenced by methodological differences before sintering [16]. Furthermore, some of the measurements show irregularities in the course of the shrinkage curve. This points to slipping and/or chipping of the samples during the measurement, which can only be detected afterwards. Since these measurements are very lengthy and the time at the instrument is limited, the measurements could unfortunately not yet be repeated.

In general, the shrinkage curves and the shrinkage rate curves, for the samples with minimal errors, are comparable to the WC-Ni dilatometer curves recorded by Roulon et al. [3]. There is a very pronounced solid-state sintering for Ni binders up to high temperatures, due to the late onset of the LPF. Then the shrinkage rate decreases and increases again quite abruptly with the occurrence of a liquid phase. The onset of LPS is, therefore, more pronounced compared to normal WC-Co systems. [3]

Despite some artefacts, trends are nevertheless recognisable when comparing the different systems:

- The binder system Ni with Cr_3C_2 as a grain-growth inhibitor (Batch 3) behaves differently than the pure Ni system (Batch 1). The splitting of the shrinkage onset characteristic of Ni binders [3] is missing. However, this effect of the Cr addition was weaker for the Ni85Fe15 binder system in Batch 2 and 4.
- Type B samples tend to show clear splitting of solid-state and liquid-phase sintering, while the ultra-fine type C samples show a very complex sintering profile. Nevertheless, for samples with 15 wt% Mo, the onset of LPS is more recognisable.

The free-C DTA curves also show irregularities for the 2nd batch. The red curves in Figure 7-23 to Figure 7-26 shows a second peak at the same temperature as the LPFT in eta-equilibrium (best seen in Figure 7-25, A). However, metallographic examination of these DTA samples did not show any detectable eta needles.

Another interesting phenomenon in the DTA can be seen in the purple eta curves: at temperatures above 1450°C, a second peak appears in all 5 wt% Mo (Figure 7-20, A) and also in some with 15 wt% Mo (Figure 3-23, C) samples. For samples with low Mo content, this can be explained by the calculated phase diagrams (appendix 7.1). For these Systems, another phase transition appears above the eta-liquidus line, where the eta phase liquifies at higher temperatures as the binder. This phase transition is missing in the calculated models of the 15 wt% Mo samples, however, this extra peak is also evident in these measurements. This can be explained by the inhomogeneity of the microstructure, as some areas of the 15 wt% Mo specimens seem to have such a low Mo content, that this additional phase transition occurs and is detectable in the DTA.

3.2.4.5 Carbon Content inside to two-phase region

Based on the LPFT of the DTA and dilatometry, it should theoretically be possible to estimate the C content within the two-phase region. For this purpose, the eta-onset temperatures from the DTA are assumed as the upper limit and the free C as the lower limit. The LPF onset of the dilatometry was determined using ImageJ software. However, the exact definition of the LPFT in the dilatometry for each specimen turns out to be problematic. For samples 1A, 2A, 2D and 4A (appendix 7.4) this is not entirely clear, as there are two onsets within these limits. Which of the two temperatures is the correct one was then chosen with good judgement. Since the limits vary for each sample, a gradual scale was designed:

$$\xi(x) = 100° \cdot \frac{x - x_0}{x_{100} - x_0} \qquad \text{Equation 3-3}$$

The two-phase C content ξ can be determined if the measured value x, which is the shrinkage LPFT, x_0 is the LPFT of the eta-region and x_{100} is the LPFT of the free-C region. This means that samples above 50° tend to contain more C, while samples below 50° are richer in W and Mo. A comparison of the specimens can be examined in Figure 3-20. The samples from batch 3 are missing because the LPFT could not be determined.

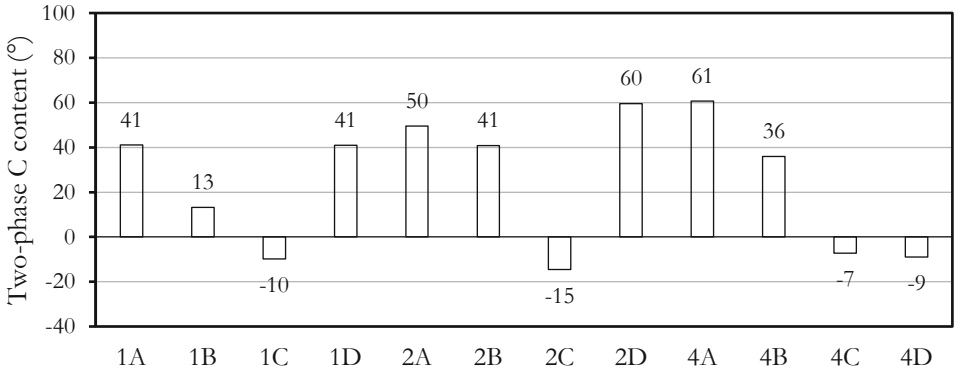

Figure 3-24: Two-phase C content of the measurable specimens

It turns out that the ultra-fine microstructure of type C shifts the onset temperature upwards during shrinkage, which falsely pushes the C content below 0°. This would mean that these samples would have eta-carbides in the microstructure, but this was ruled out during the metallographic examination. Sample 4D can be regarded as an outlier, since here too the LPFT is only vaguely discernible in the shrinkage rate. Nevertheless, for the other samples, the experiment yielded acceptable results. With a corresponding number of measurements and improvements in the performance of dilatometry and evaluation, it could be possible to measure the C content of the Ni-based binder inside the two-phase window.

3.3 Mechanical properties

Figure 3-25 shows a comparison of the Ni-based (round shape) and 85Ni15Fe-based (diamond shape) cemented carbides with the Co-binder hardmetals [27] (black-doted line). Each hard phase is represented by a different colour: A (red), B (yellow), C (blue) and D (green). Co-binder systems are represented by a straight line for the WC-Co systems and open circles for (W,Mo)C-Co samples. Specimens with added Cr_3C_2 have black-edged symbols.

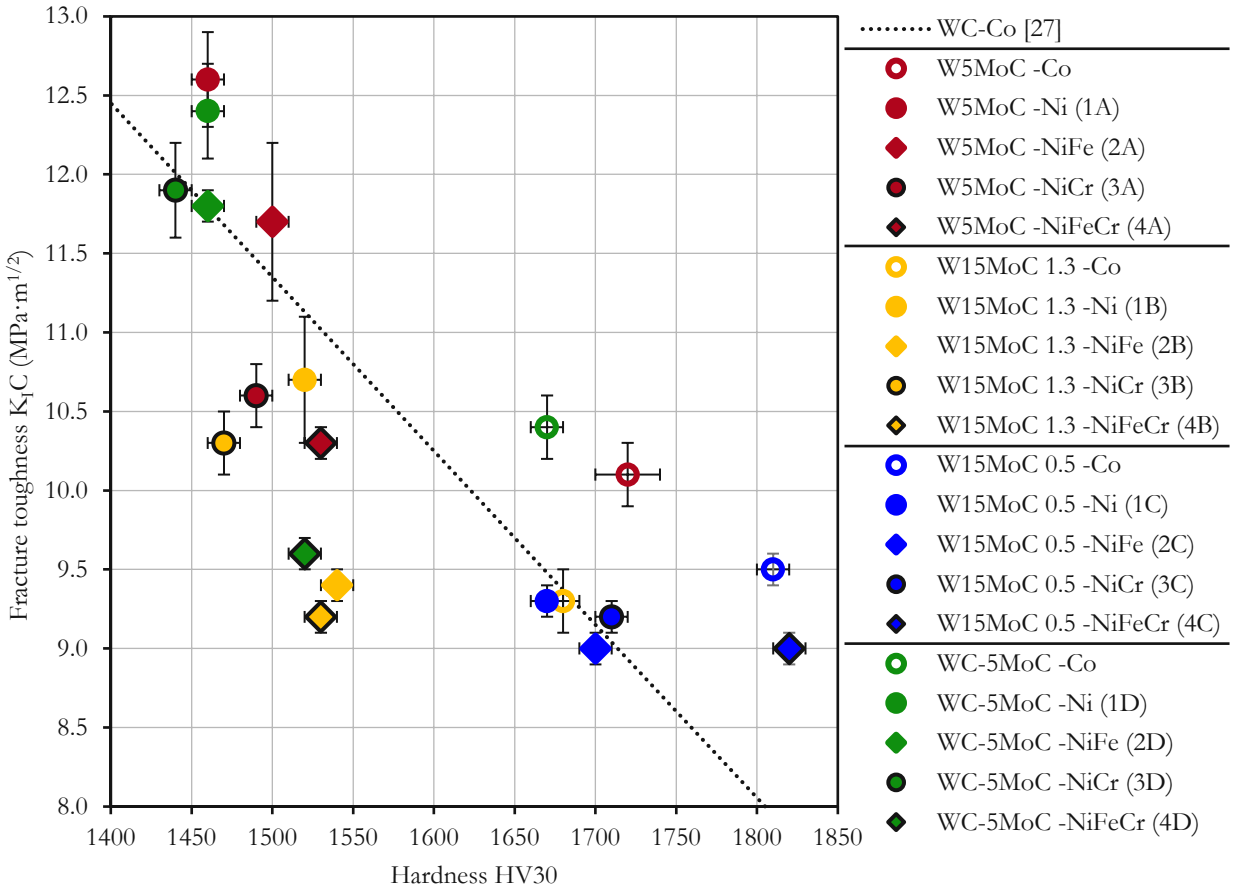

Figure 3-25: Fracture toughness against the hardness of all samples in comparison with Co-binder samples of the corresponding hard phase and common WC-Co [27]

The trend of the data points shows that the general effect of the Ni-based binder systems is a reduction of hardness but at the same time an increase in fracture toughness when compared with the Co binder. The trends for each hard phase are as follows:

- The samples of the hard-phase type A (red) lose up to 260 points HV30 compared to their Co-binder system but gain some toughness, which corresponds to the normal trend of the WC-Co systems (see black line). However, it is noticeable that the samples without a grain-growth inhibitor perform better than those with chromium carbide added. The addition of the inhibitor comes with a bad trade-off, as the loss in toughness is greater than the increase in hardness.

- Type B (yellow) is the worst-performing hardmetal which is a result of the persisting problem of residual porosity. This takes a toll on both hardness and toughness. Even the sample with good porosity (1B) barely comes within the range of the WC-Co curve, which means that the sintering behaviour of this particular hard phase is very unoptimized.
- Type C (blue) has increased hardness thanks to its ultra-fine microstructure which is comparable to the common Co-binder systems. Interestingly the binder system NiFeCr (specimen 4C → W15MoC 0.5 - NiFeCr in Figure 3-25) has an exceptional hardness which is commensurate with the Co-System, making this specimen an interesting candidate for further investigations.
- Type D (green) achieves results similar to type A, which proves that the pre-alloyed powders have equal, if not better properties than the powder blends. The inferior performance of the "NiFeCr" (specimen 4D) is the result of the high residual porosity of this sample (Figure 3-10).
- If considering the differences in the binder systems, it can be seen that binder system 3 (NiCr) has generally performed the worst, which means that this combination of NiCr and Mo in the binder has rather negative effects. Yih et. al. [9] noted similar results for the addition of Cr to the Ni binder.

In conclusion, the mechanical properties of these new hard-phase powders are comparable to those of conventional WC-Co systems. Even samples with high Mo content can achieve excellent results if the microstructure is adjusted accordingly. Considering the results the development of the microstructure has to be investigated and improved for each system individually, due to the chemically complex composition. Within the scope of this work, it was only possible to work with chromium carbide as a grain-growth inhibitor, leaving many possible candidates [1, 9] on the Table. This inhibitor had negative effects for the 5 wt% Mo samples, while it significantly improved the properties for the ultrafine microstructure. This could be because of the high Mo content in the binder, the addition of further components displaces parts of Mo in the binder and promotes the solution and re-precipitation process during liquid phase sintering, which leads to a better microstructure (see Figure 3-16).

4 SUMMARY

In this work, the production and properties of new (W,Mo)C cemented carbides with 2 alternative binder phases were investigated. It was possible to produce hardmetals with Co-free binder systems of good quality and with mechanical properties in close range of the common industrial WC-Co systems. However, the investigations also showed that the high Mo content influences the chemistry and the sintering behaviour of the samples. Depending on the combination of Mo content, grain size and additives, this can have both positive and negative effects.

Thermo-Calc™ and the DTA were then used to investigate and compare the thermodynamics of the systems. It was found that the more complicated the system, the more accurate the Thermo-Calc™ calculations is. For example, deviations of up to 50 K were noted for the pure nickel system (binder 1), while the NiFeCr-binder system (binder 4) deviated by a maximum of 10 K (Figure 3-2, page 13). CALPHAD calculations done by Zhang et al. [23] came to similar results (Figure 3-3 and Figure 3-4, page 14)

The Thermo-Calc™ diagrams correctly predicted the occurrence of another liquid-phase formation in the η-curves of the $(W_{0.91}Mo_{0.09})C$ samples (Figure 7-20, page 47). Parts of the η-phase in samples with low Mo content may melt at temperatures above 1450°C (Figure 7-4, page 40). This phenomenon is also visible in the DTA for $(W_{0.76}Mo_{0.24})C$ samples, although less pronounced. However, in the Thermo-Calc™ calculation of these samples, this phase transition does not occur at all. On this occasion, the CALPHAD method may be only partially mistaken: both powder XRD and SEM images document a pronounced inhomogeneity in the microstructure, i. e. the equilibrium state has not been reached [11-13]. Thermo-Calc™ assumes a complete thermodynamic equilibrium in its calculations, hence the phase transitions, are not calculated accurately.

The powder XRD investigation also showed that the Mo content has a great influence on the lattice parameters of the binder (Figure 3-5, page 15). For the same binder system, the binder peaks show a shift for each hard phase, while the reflections of the hard phases remain constant. Nevertheless, a quantitative investigation of the binder with the help of the Rietveld refinement could not be achieved.

The very clear core-rim structure of some grains shown in the SEM images cannot be investigated using XRD. A closer look at the hard-phase reflections shows that they are broadened (Figure 3-6, page 16), which indicates a gradient of the Mo concentration in the individual grains. Even if this core structure differs, it was shown that those peaks would probably be lost in the diffractogram due to the low intensity and would therefore be undetectable.

The problem of high residual porosity was successfully removed for almost all samples by extending the initial grinding time (to at least 72h) and raising the sintering temperature to 1480°C. Only samples of hard-phase-type B showed a persistent residual porosity (Figure 3-12, page 22), whereby an interesting phenomenon could be documented. For sample 1B, it was possible to reduce the porosity unintentionally, by going beyond the free-C equilibrium through C doping. The subsequent reduction of the C content through employing multiple re-grinding sessions had an unexpected effect on the microstructure. 2C and 4D (Figure 3-10, page 20) were two outliers concerning the porosity. However, based on other results of dilatometry, differential thermal analysis (DTA) and hardness, it is also possible that certain combinations of the binder and hard phase lower the sintering activity.

The sintering behaviour was also investigated using DTA and dilatometry. The DTA supported the detection of the onset of liquid-phase sintering and enabled an assessment of the C content within the C window. These investigations also revealed a very complex picture of the sintering behaviour. As is typical for Ni-binder systems, they show a recognisable temporal separation between solid and liquid phase sintering. [3] Only binder system 3 (NiCr) does not show this behaviour. For these samples, a continuous transition was measured, which in turn is a possible cause for the somewhat inferior mechanical properties in the hardness test.

The mechanical tests show that these hardmetal systems are indeed capable of keeping up with the usual WC-Co systems, provided that the porosity can be brought under control and the appropriate grain-growth inhibitor has been found. The most promising system from this work is sample 4C (W15MoC 0.5µm -NiFeCr), which

stood out for its exceptional hardness with little loss of toughness (Figure 3-25, page 31). However, an actual statement about the applicability of these systems can only be made after a wear resistance test. Additionally, the weight reduction through the replacement of up to 24% W with Mo should not be disregarded. The density can be reduced by about 1 g/cm³ which can make an enormous difference on an industrial scale with regards to the price.

Table 4-1: Summary of the results for each sample

Desig-nation	Hard phase	Binder	Density (g/cm³)	d10-d90 slope	Porosity (%)	Porosity Norm	HV30	K_{Ic} (MPa·m$^{1/2}$)
1A	W5MoC	Ni	14.12	101	0.01	A02	1460	12.6
1B	W15MoC	Ni	12.94	134	0.02	A02	1520	10.7
1C	W15MoC	Ni	13.06	135	0.01	A02	1670	9.3
1D	W5MoC	Ni	14.00	106	0.02	A02	1460	12.4
2A	W5MoC	NiFe	14.08	190	0.00	A02	1500	11.7
2B	W15MoC	NiFe	12.95	99	0.44	A06	1540	9.4
2C	W15MoC	NiFe	13.01	205	0.08	A04	1700	9.0
2D	W15MoC	NiFe	14.03	151	0.02	A02	1460	11.8
3A	W5MoC	NiCr	14.05	210	0.02	A02	1490	10.6
3B	W15MoC	NiCr	13.01	134	0.53	A06	1470	10.3
3C	W15MoC	NiCr	13.09	165	0.02	A02	1710	9.2
3D	W5MoC	NiCr	14.01	168	0.00	A02	1440	11.9
4A	W5MoC	NiFeCr	13.83	182	0.04	A02	1530	10.3
4B	W15MoC	NiFeCr	12.86	120	1.02	A08	1530	9.2
4C	W15MoC	NiFeCr	12.91	230	0.02	A02	1820	9.0
4D	W5MoC	NiFeCr	13.95	140	0.19	A04	1520	9.6

5 ACKNOWLEDGEMENTS

This work has been performed at the Institute of Chemical Technology and Analytics and the Vienna University of Technology. I would like to announce my sincere appreciation for the opportunity to carry out this work during a pandemic and the chance to finish my studies in this very unusual situation. I would especially like to thank my supervisors Prof. Dr. Walter Lengauer and Dipl.-Ing. Markus Fürst, who accompanied me through my work with a lot of patience and effort. Despite tedious time regulations and complicated hygiene measures, they never gave up on fighting and arranging for as much time as possible in the laboratory. Thank you, Walter, for your availability and your way of explaining these complicated topics thoroughly. Thank you, Markus, for your dedication in explaining the processes, equipment, time management and problem-solving in the lab, often at the expense of your own scientific work. Thank you, to my colleague and friend, Johannes Maschke, for a great time in the lab during these uncertain times.

At this point, I would also like to thank my family and my parents, Ulrike and Franz. Without their unceasing patience, generosity and mental and financial support over the past years, this study would have been much more challenging. I would also like to thank my partner Katrin. Thank you, for being with me throughout my studies and for giving me comfort and love.

Finally, I would like to thank all my fellow students and friends during the entire study period, especially the "Männer von Flake": Michael, Markus, Johannes, Florian, Victor, Pontus, Felix and once again Markus. It was your constant camaraderie that made my studies what they are.

6 REFERENCES

1. D. Mari, L. Llanes, and C.E. Nebel, *Hardmetals*. Comprehensive Hard Materials, ed. V.K. Sarin. Vol. 1. 2014: Elsevier (UK).
2. *Critical Raw Materials Resilience: Charting a Path towards greater Security and Sustainability*. 2020, The European Economic and Social Committee and the Committee of the Regions.
3. Z. Roulon, J.-M. Missiaen, and S. Lay, *Shrinkage and microstructure evolution during sintering of cemented carbides with alternative binders*. International Journal of Refractory Metals and Hard Materials, 2021. **101**: p. 105665.
4. *Worldwide strategic resources*. Statista Dossier on global strategic resources, 2019.
5. B.K. Sovacool, *The precarious political economy of cobalt: Balancing prosperity, poverty, and brutality in artisanal and industrial mining in the Democratic Republic of the Congo*. The Extractive Industries and Society, 2019. **6**(3): p. 915-939.
6. Y. Foucaud, L. Filippov, I. Filippova, and M. Badawi, *The Challenge of Tungsten Skarn Processing by Froth Flotation: A Review*. Frontiers in Chemistry, 2020. **8**.
7. E. Rudy, B.E. Kieffer, and E. Baroch, *HfN Coatings for Cemented Carbides and New Hard Facing Alloys on the Basis (Mo, W)C-(Mo,W)2C*. Planseeber. Pulvermet., 1978. **26**.
8. J. Schuster, E. Rudy, and H. Nowotny, *Die "MoC"-Phase mit WC-Struktur*. Monatshefte für Chemie, 1976. **107**.
9. S. Yih, S.A. Worcester, and E. Rudy, *Cemented Carbides Containing Hexagonal Molybdenum*. 1977, Teledyne Industries, Inc.: USA.
10. C. Liu, M. Komatsu, A. Nino, S. Sugiyama, and H. Taimatsu, *Preparation of WC-MoC Ceramics and their Mechanical Properties*. Journal of the Japan Society of Powder and Powder Metallurgy, 2012. **59**(8): p. 479-483.
11. K. Shi, V. Schwarz, and W. Lengauer, *Preparation and Properties of (W,Mo)C powders and (W,Mo)C-Co cemented carbides*, in *Proc. 19th Plansee Seminar*. 2017, Plansee Group: Reutte (A).
12. V. Schwarz, K. Shi, and W. Lengauer, *Metallurgy and Properties of Mo-doped WC-Co and (W,Mo)C-Co Hardmetals*, in *Proc. WorldPM 2016*. 2016, EPMA: Hamburg (D).
13. T.J. Jewett, *Effects of doping WC-Co hardmetals with Mo and Mo2C*. Plansee Seminar, 2017. **19**.
14. V. Dalbauer and T. Jewett, *Effect of Mo and Mo2C Additions on the Micostructure of Sintered WC-Co Components*. Euro PM2014, 2014.
15. L. Tang, P. Wang, T.E. Graedel, S. Pauliuk, K. Xiang, Y. Ren, and W.-Q. Chen, *Refining the understanding of China's tungsten dominance with dynamic material cycle analysis*. Resources, Conservation and Recycling, 2020. **158**: p. 104829.
16. A. Petersson, *Cemented Carbide Sintering : Constitutive Relations and Microstructural Evolution*. 2004, Materialvetenskap: Stockholm. p. viii, 37.
17. A. Kopczynska and G.W. Ehrenstein, *Oberflächenspannung von Kunstoffen Messmethoden am LKT*. 2017, Friedrich-Alexander-Universität: Erlangen-Nürnberg.
18. R. Kieffer, P. Ettmayer, and B. Lux, *Molybdänmetall und Molybdäncarbid in Hartmetallen*. METALL, 1979. **33**.
19. W.D. Schubert, P. Ettmayer, B. Lux, and W. Ohlsson, *Phase equilibria in the Co-Mo-W-C and Ni-Mo-W-C systems*. High Temperatures - High Pressures, 1982. **V 14(1)**(N 1): p. 87-100.
20. N. Akmoran, *Untersuchungder Löslichkeit von (Mo,W)C in Co und Ni*. 1984.
21. M. Moien and E. Alizadeh, *Investigation of (Mo, W)C Based Cemented Carbides*. Asian Journal of Chemistry, 2006. **18**(2).

22. Internetchemie.info. *Wasser-Dichtetabelle*. 25.05.2021 14.12.2020; Available from: https://www.internetchemie.info/chemie-lexikon/daten/w/wasser-dichtetabelle.php.

23. C. Zhang, H. Yin, J. Lv, Y. Du, Z. Tan, and Y. Liu, *Thermodynamic investigation of phase equilibria on the (W,Mo)C-(Co,Ni) cemented carbides*. Calphad, 2019. **67**.

24. H. Krischner, *Einführung in die Röntgen-Feinstruktur-Analyse*. 1987: Vieweg.

25. J.H. Hubbell and S.M. Seltzer. *X-Ray Mass Attenuation Coefficients*. July 2004 [cited 2021 29.07.; Available from: https://physics.nist.gov/PhysRefData/XrayMassCoef/tab3.html.

26. B. Wittmann, W.-D. Schubert, and B. Lux, *WC grain growth and grain growth inhibition in nickel and iron binder hardmetals*. International Journal of Refractory Metals and Hard Materials, 2002. **20**(1): p. 51-60.

27. Z.Z. Fang, *Correlation of transverse rupture strength of WC–Co with hardness*. International Journal of Refractory Metals and Hard Materials, 2005. **23**(2): p. 119-127.

7 APPENDIX

7.1 Thermo-Calc™ Calculations

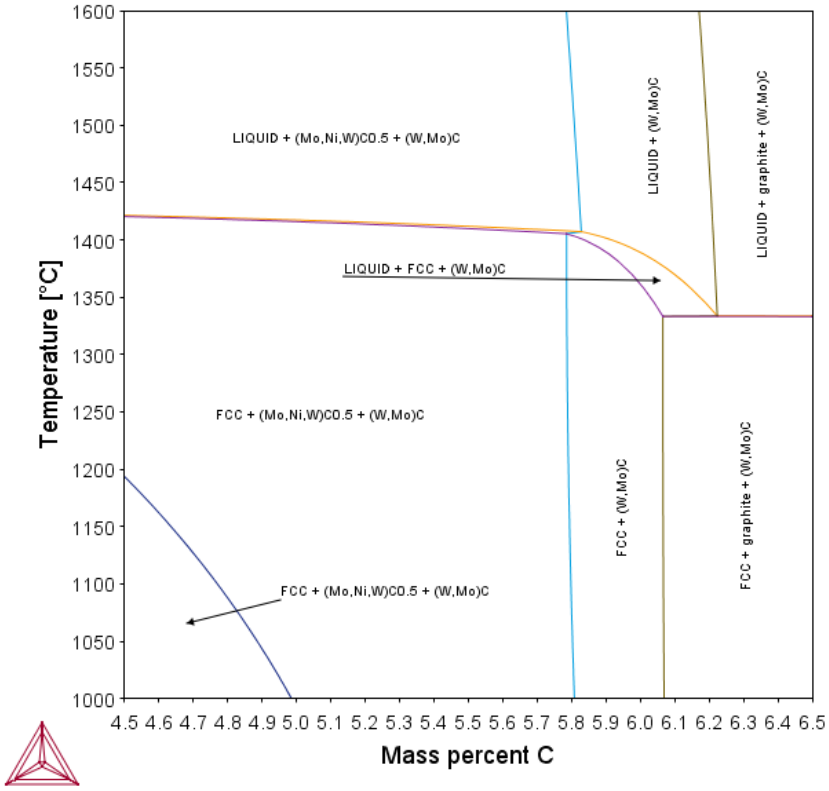

Figure 7-1: Calculated phase diagram of the $(W_{0.76}Mo_{0.24})C$ - Ni system

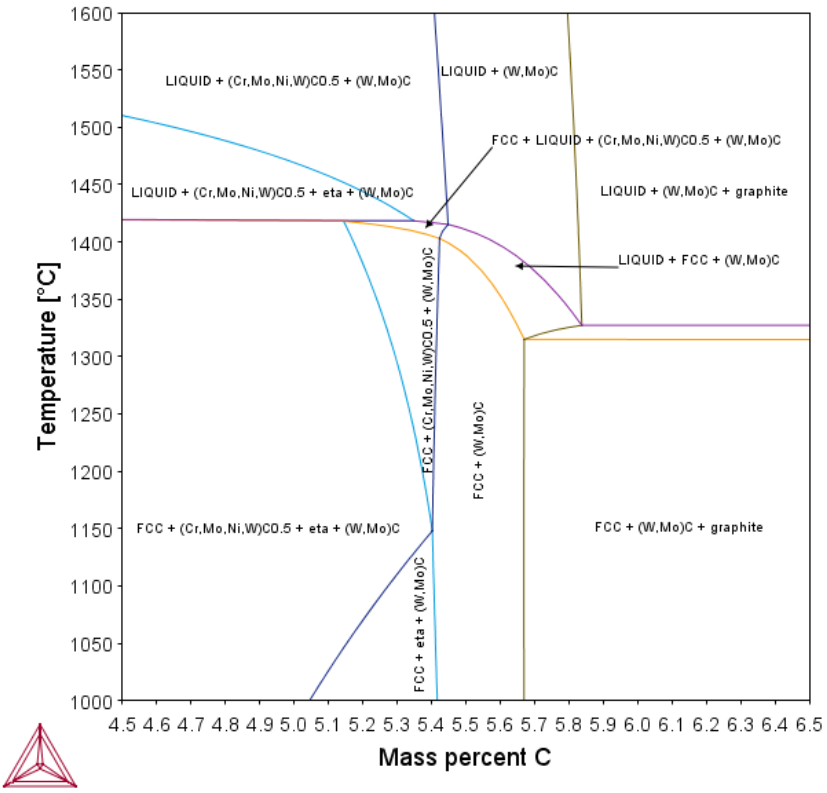

Figure 7-2: Calculated phase diagram of the $(W_{0.91}Mo_{0.09})C$ - NiCr system

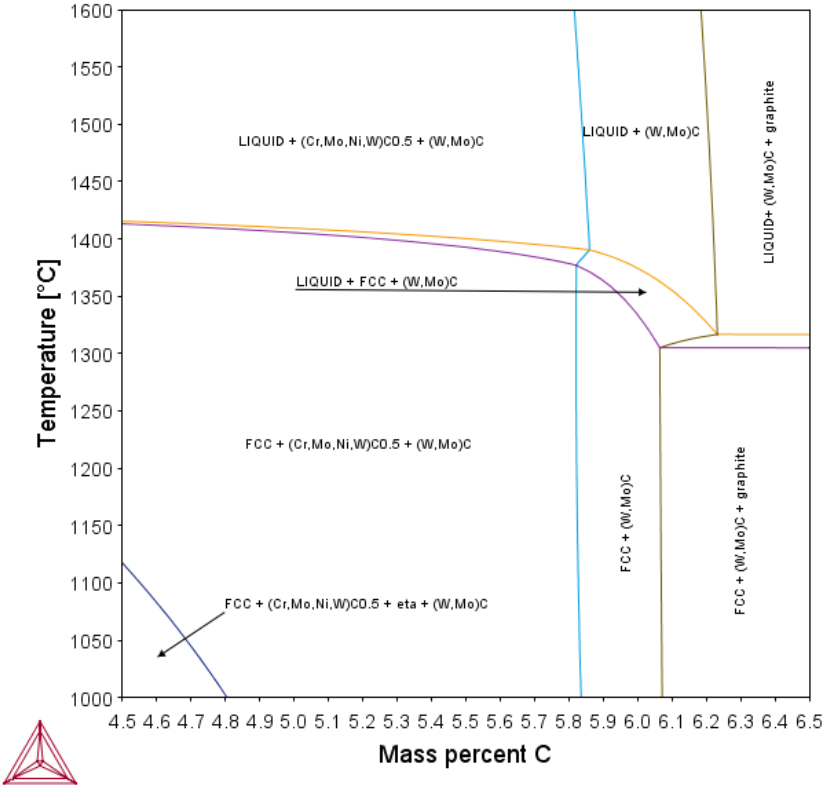

Figure 7-3: Calculated phase diagram of the $(W_{0.76}Mo_{0.24})C$ - NiCr system

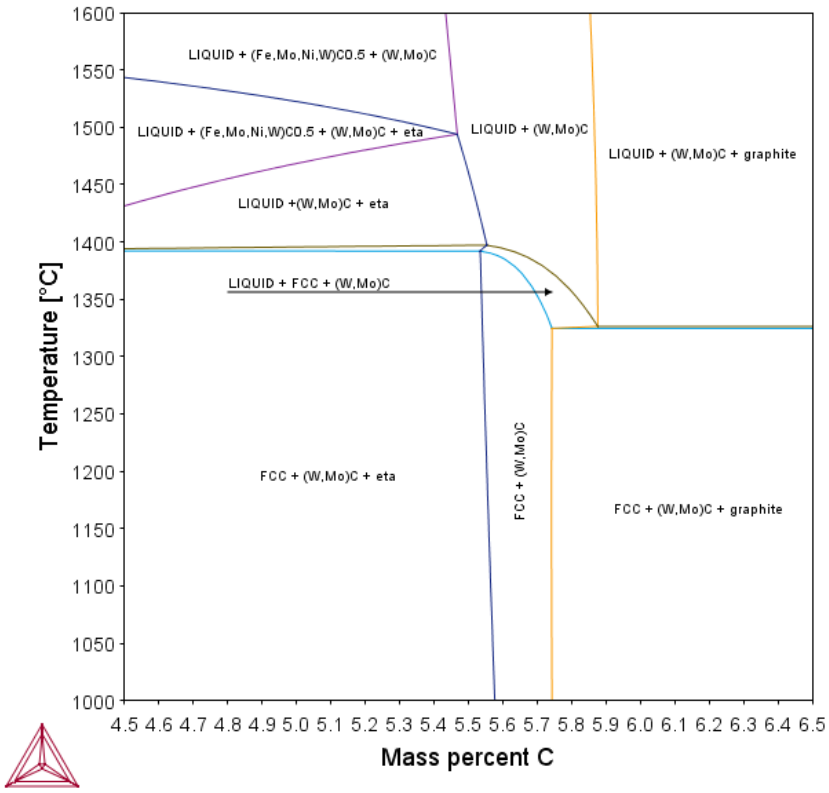

Figure 7-4: Calculated phase diagram of the $(W_{0.91}Mo_{0.09})C$ – Ni85Fe15 system

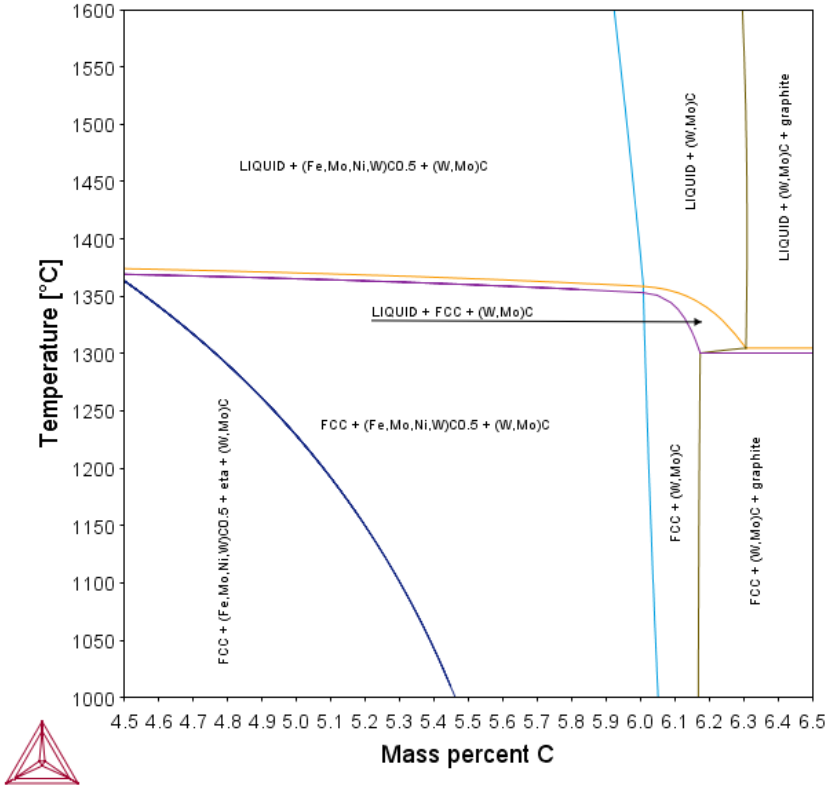

Figure 7-5: Calculated phase diagram of the $(W_{0.76}Mo_{0.24})C$ – Ni85Fe15 system

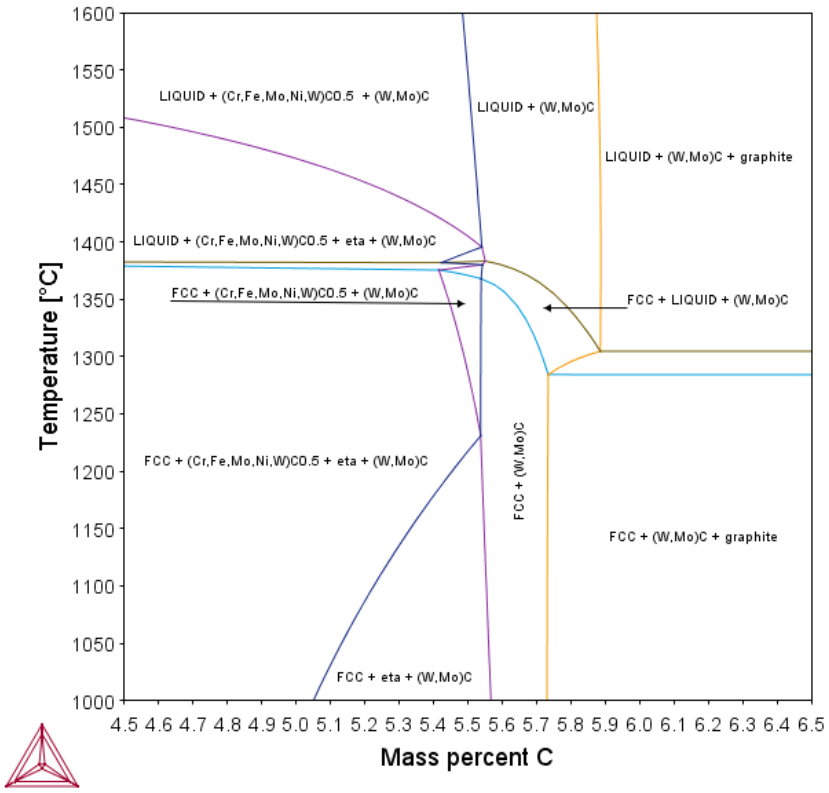

Figure 7-6: Calculated phase diagram of the $(W_{0.91}Mo_{0.09})C$ – Ni85Fe15Cr system

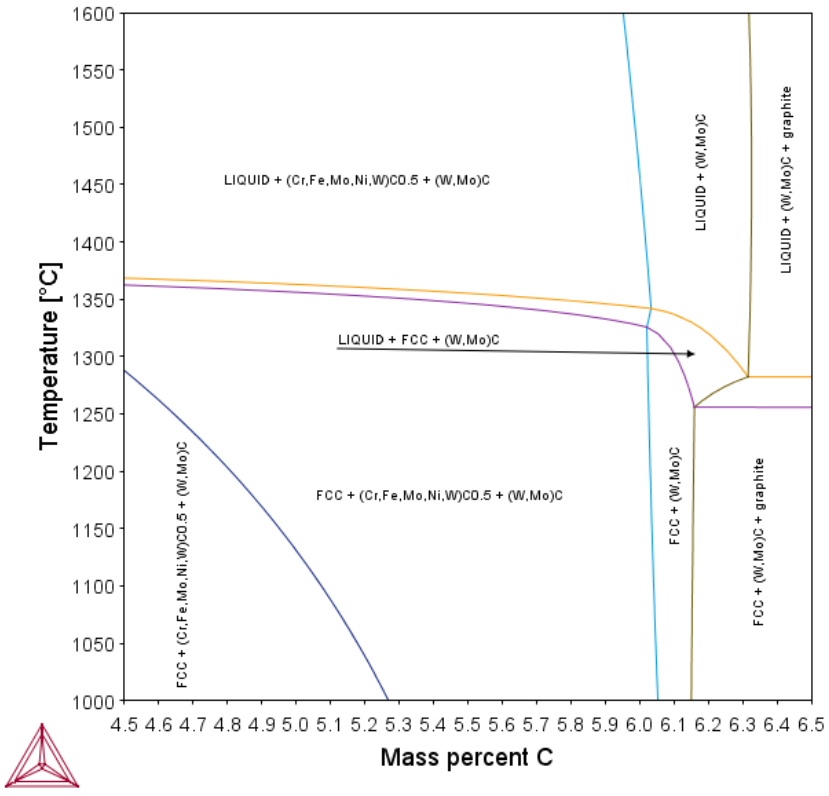

Figure 7-7: Calculated phase diagram of the $(W_{0.76}Mo_{0.24})C$ – Ni85Fe15Cr system

7.2 Powder XRD

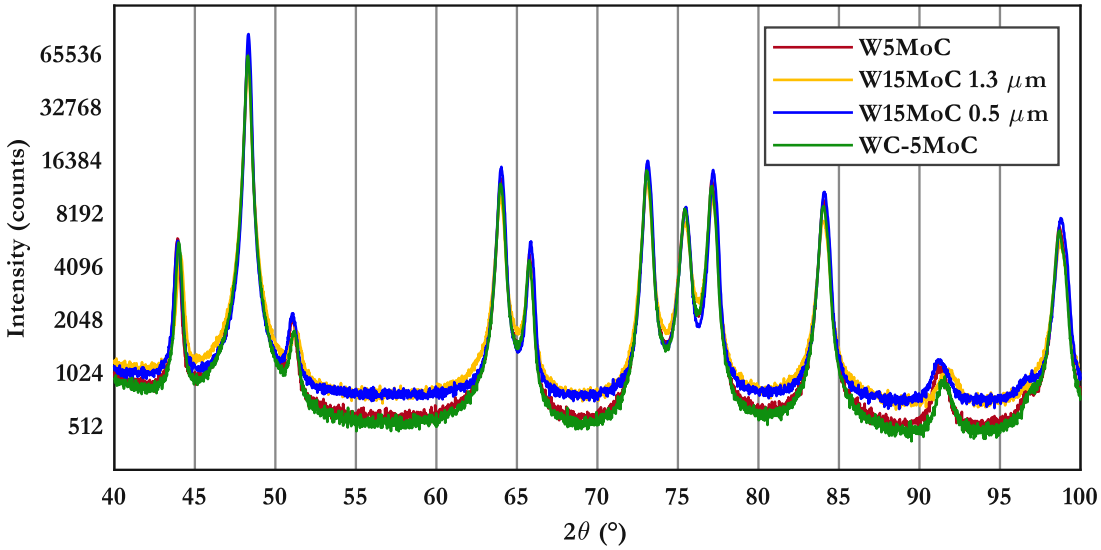

Figure 7-8: Comparison of the different hard phases of binder 2 (Ni85Fe15) from 40° to 100° 2θ

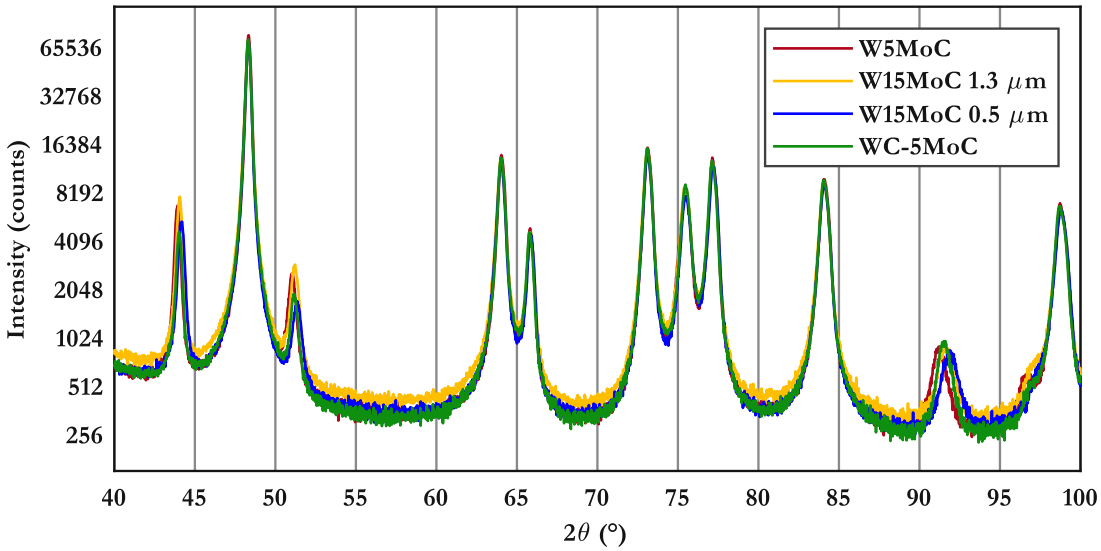

Figure 7-9: Comparison of the different hard phases of binder 3 (NiCr) from 40° to 100° 2θ

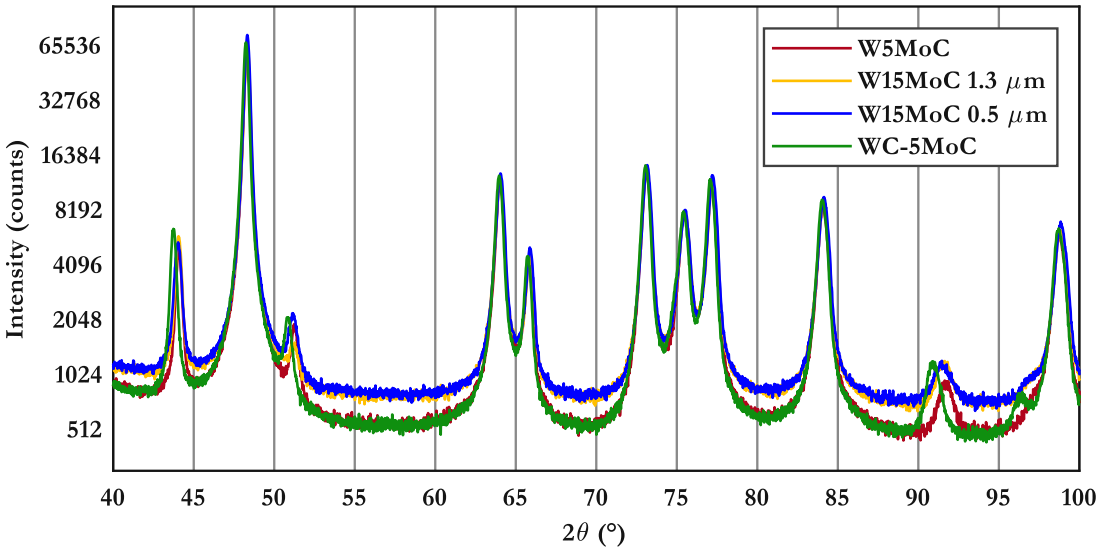

Figure 7-10: Comparison of the different hard phases of binder 4 (Ni85Fe15Cr) from 40° to 100° 2θ

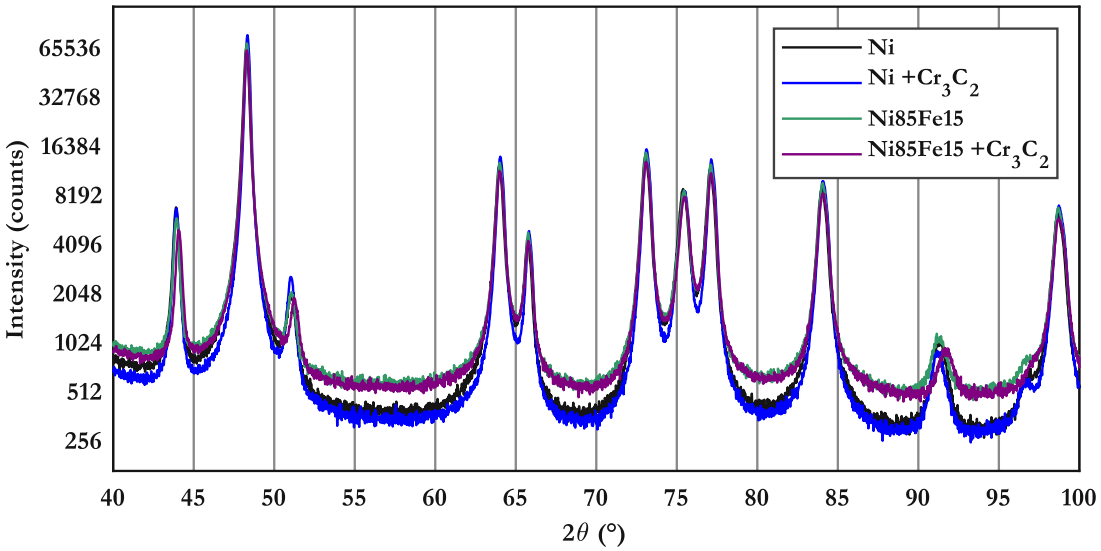

Figure 7-11: Comparison of the different binder phases of hard phase-type A (W5MoC)

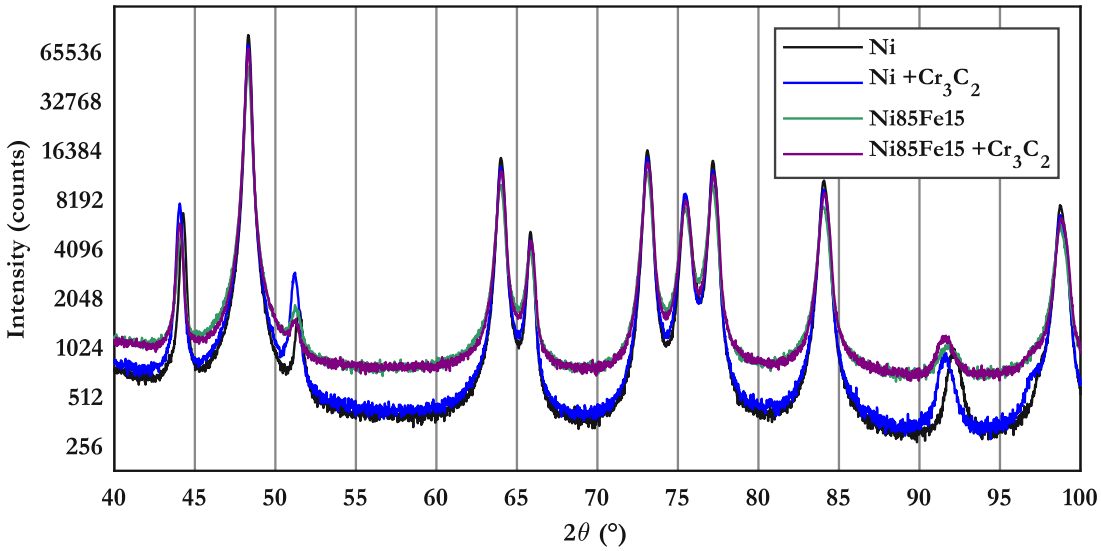

Figure 7-12: Comparison of the different binder phases of hard phase-type B (W15MoC 1.3 µm)

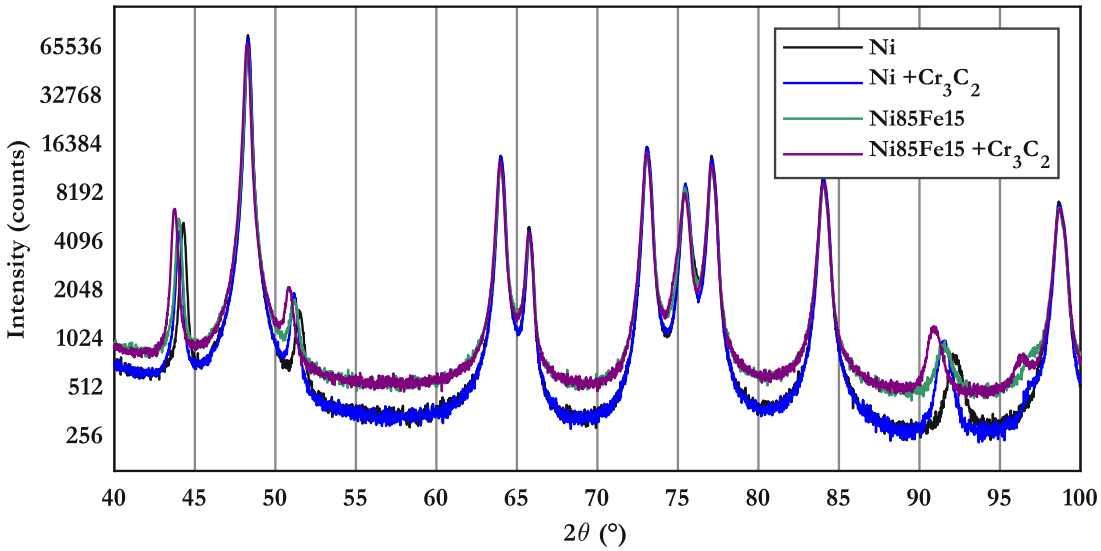

Figure 7-13: Comparison of the different binder phases of hard phase-type D (WC-5MoC)

7.3 Grain-size distribution

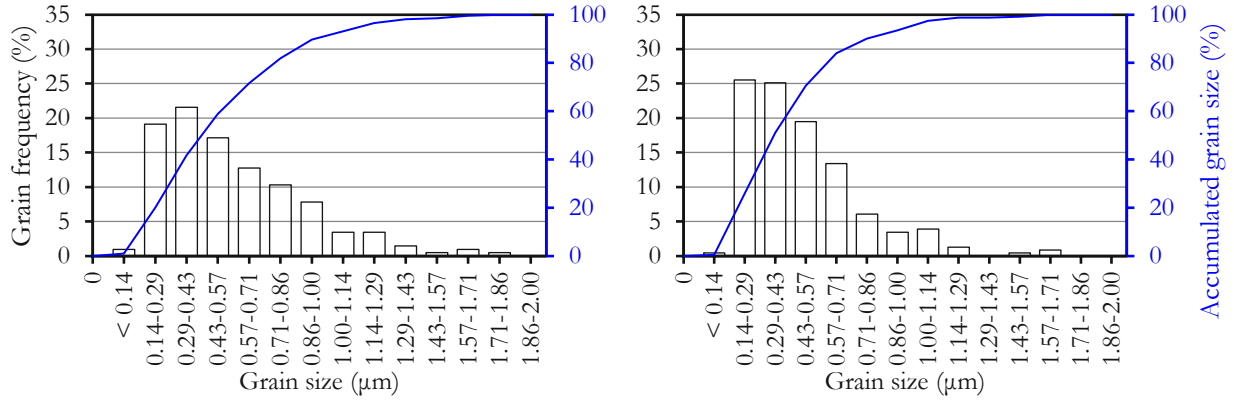

Figure 7-14: Comparison of the grain-size distribution of samples 1A (left) and 3A (right)

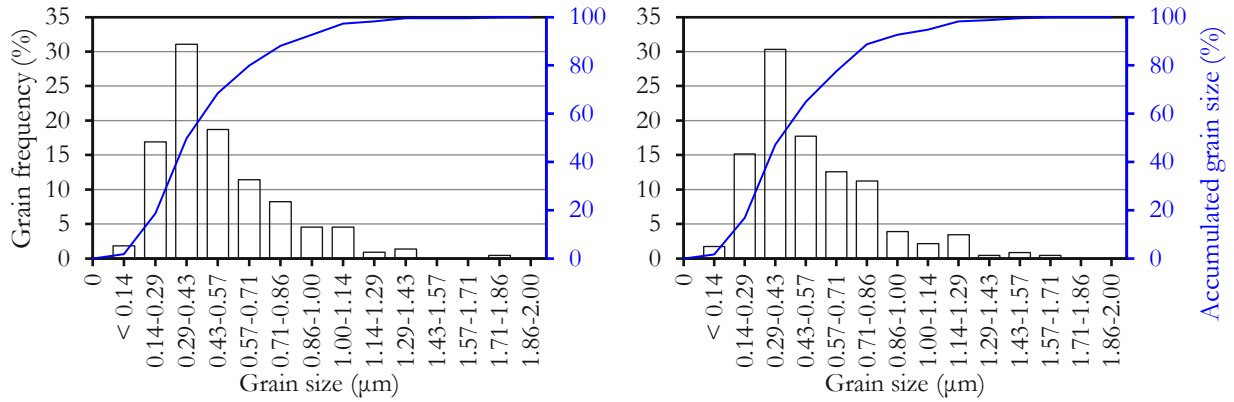

Figure 7-15: Comparison of the grain-size distribution of samples 1B (left) and 3B (right)

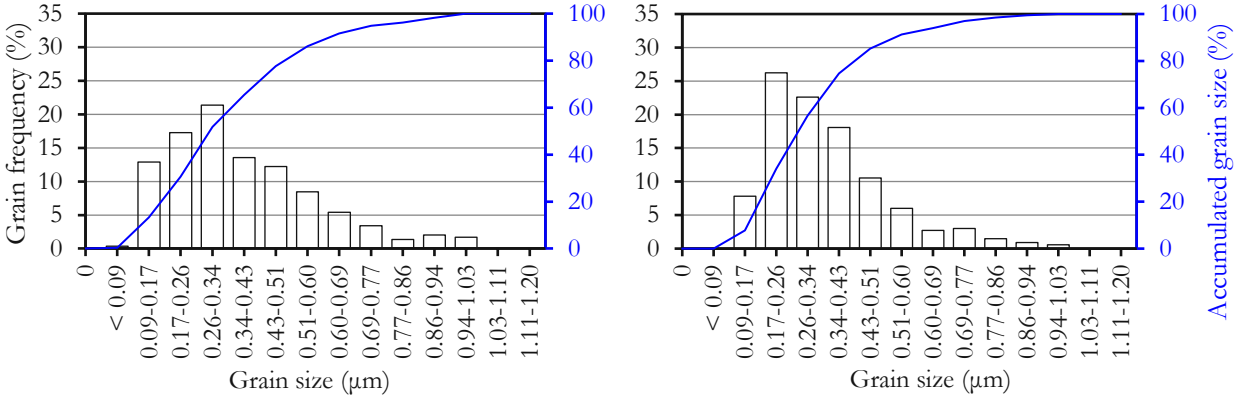

Figure 7-16: Comparison of the grain-size distribution of samples 1C (left) and 3C (right)

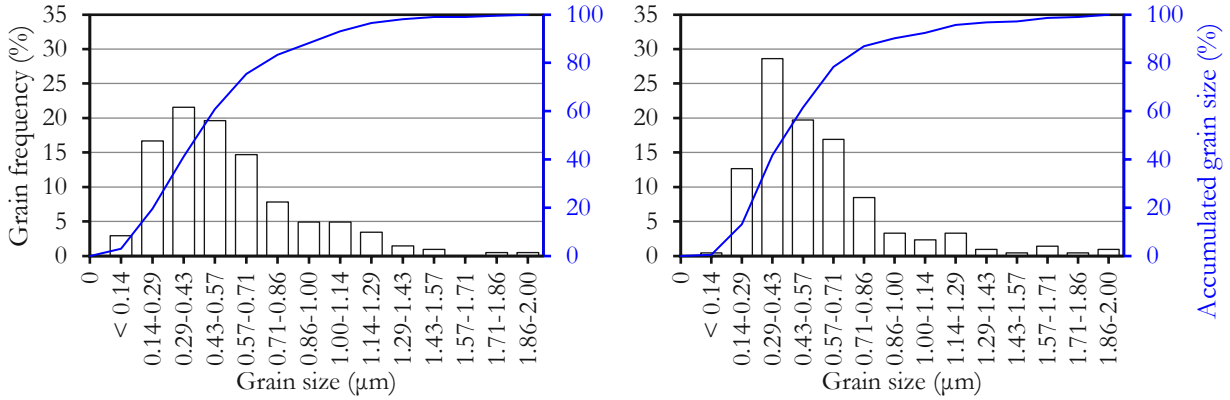

Figure 7-17: Comparison of the grain-size distribution of samples 1D (left) and 3D (right)

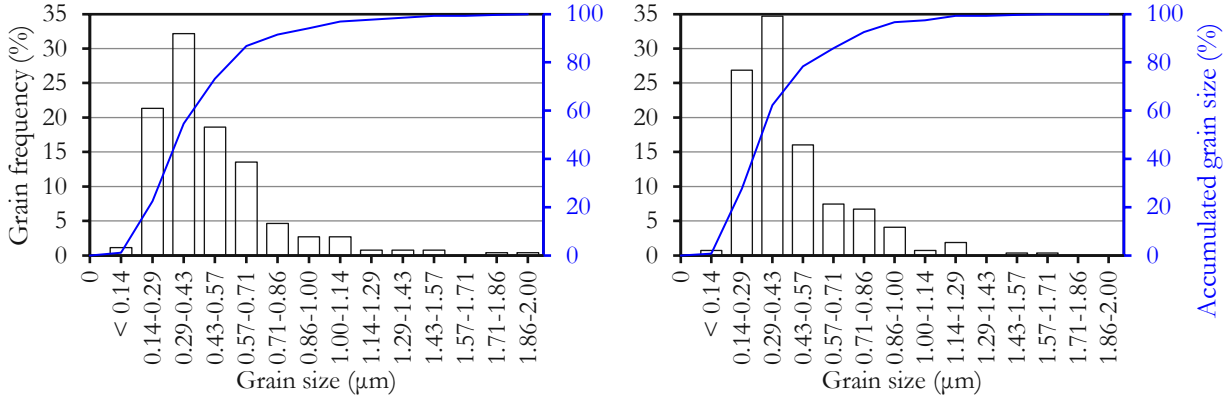

Figure 7-18: Comparison of the grain-size distribution of samples 2A (left) and 4A (right)

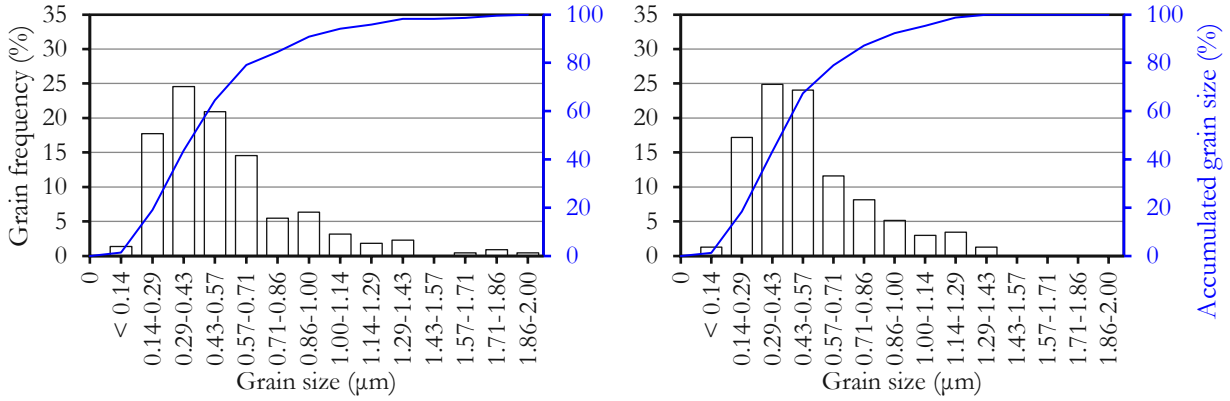

Figure 7-19: Comparison of the grain-size distribution of samples 2D (left) and 4D (right)

7.4 Dilatometry

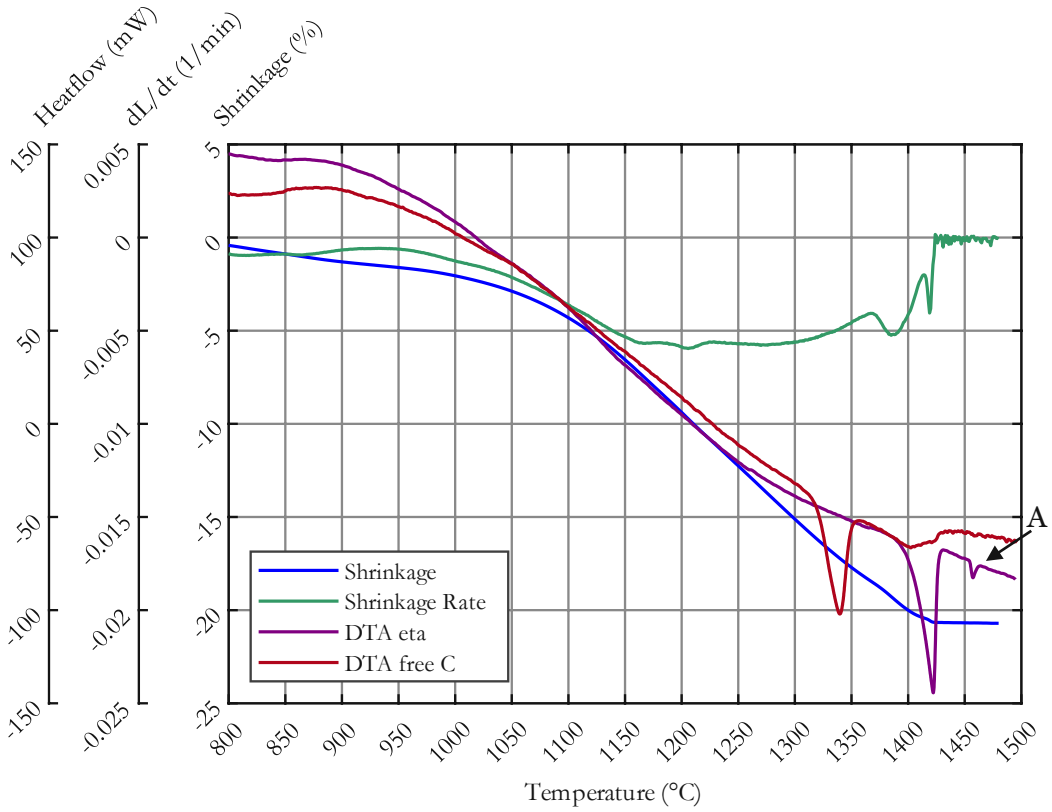

Figure 7-20: Combined diagram of dilatometer and DTA plotted against the temp. of sample 1A

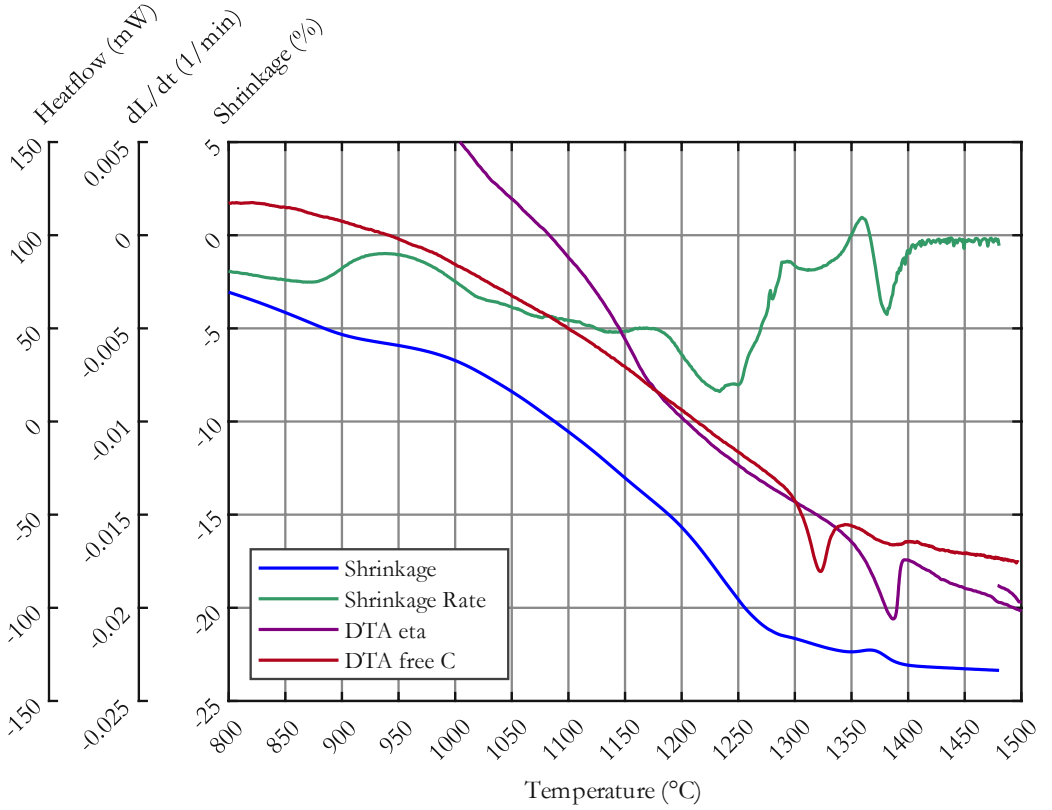

Figure 7-21: Combined diagram of dilatometer and DTA plotted against the temp. of sample 1C

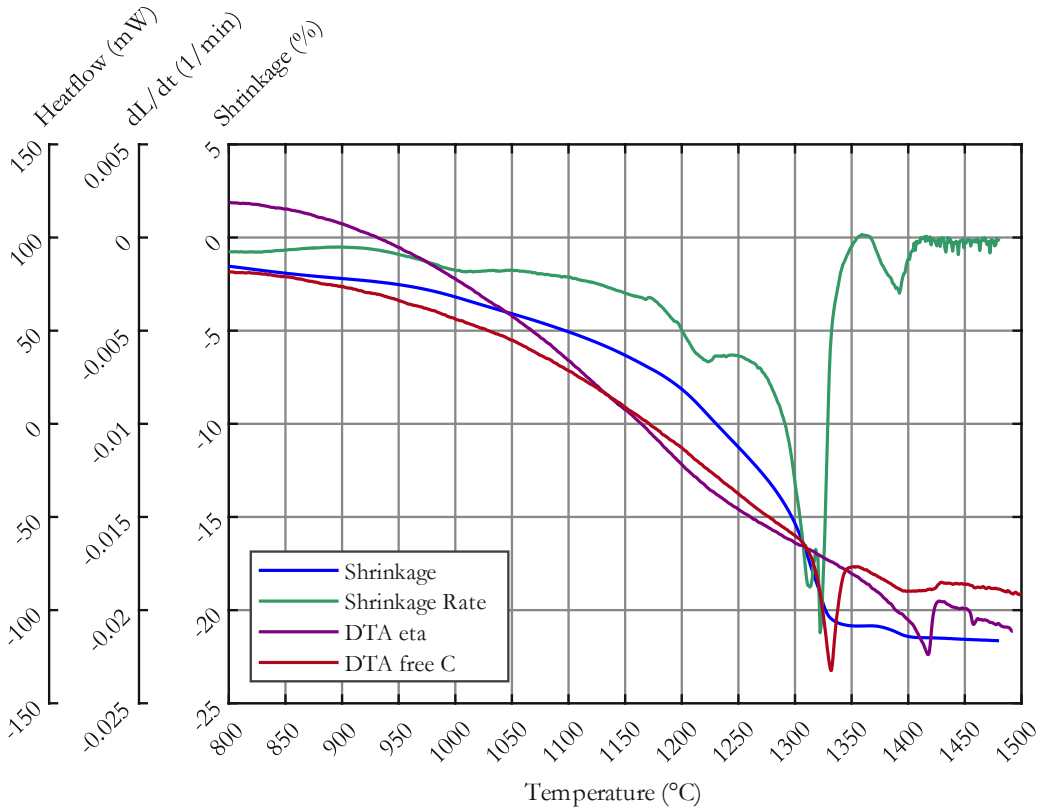

Figure 7-22: Combined diagram of dilatometer and DTA plotted against the temp. of sample 1D

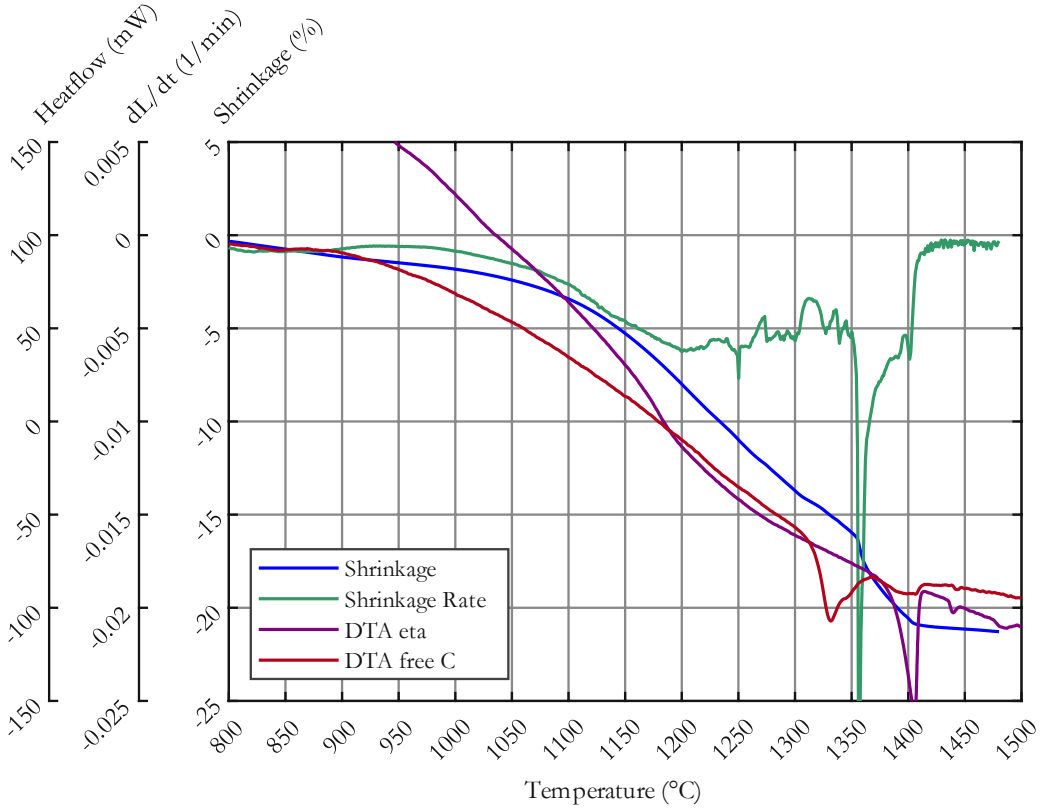

Figure 7-23: Combined diagram of dilatometer and DTA plotted against the temp. of sample 2A

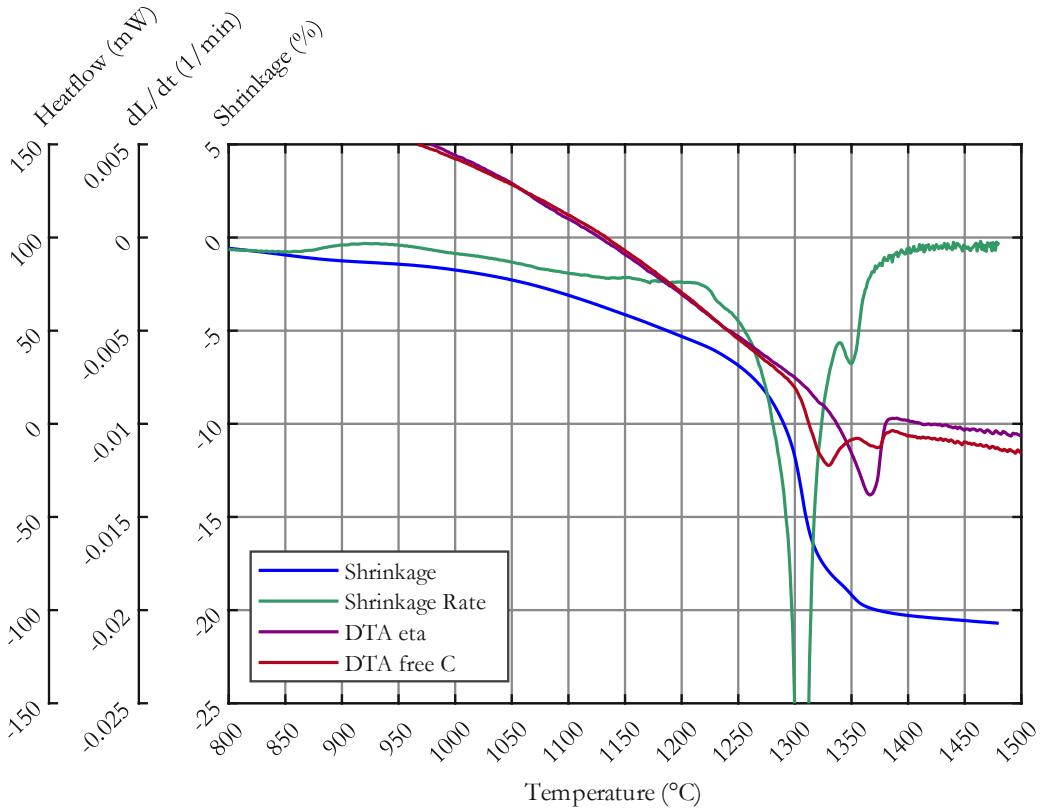

Figure 7-24: Combined diagram of dilatometer and DTA plotted against the temp. of sample 2B

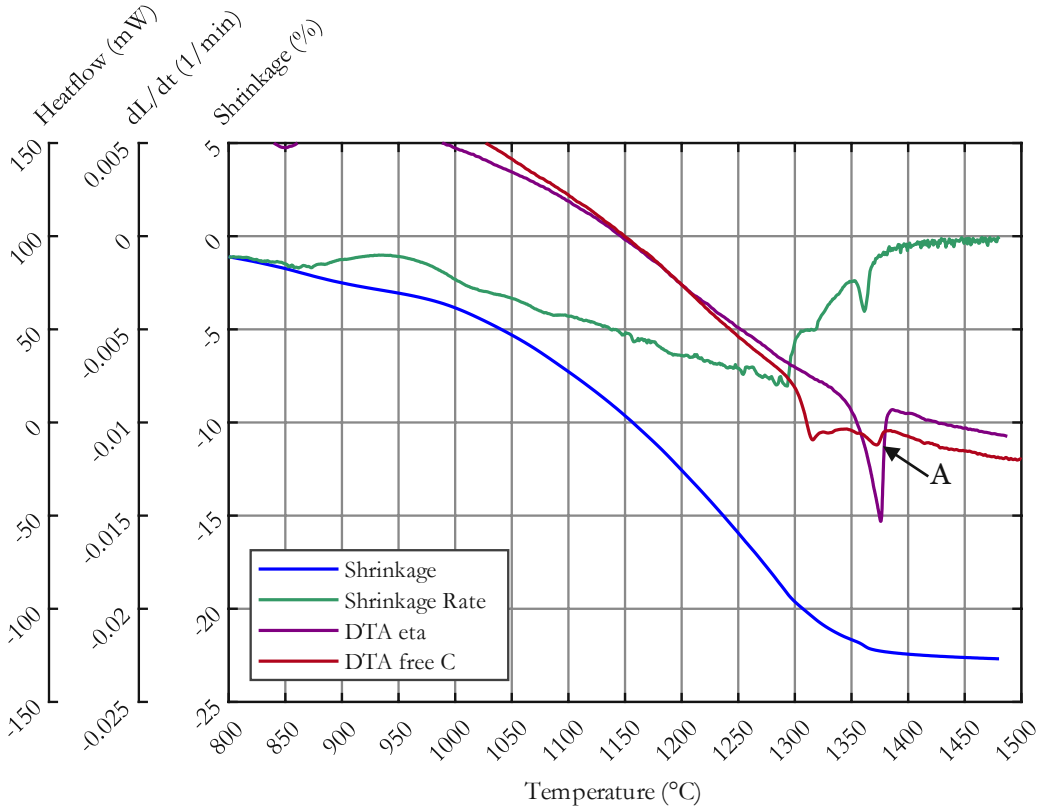

Figure 7-25: Combined diagram of dilatometer and DTA plotted against the temp. of sample 2C

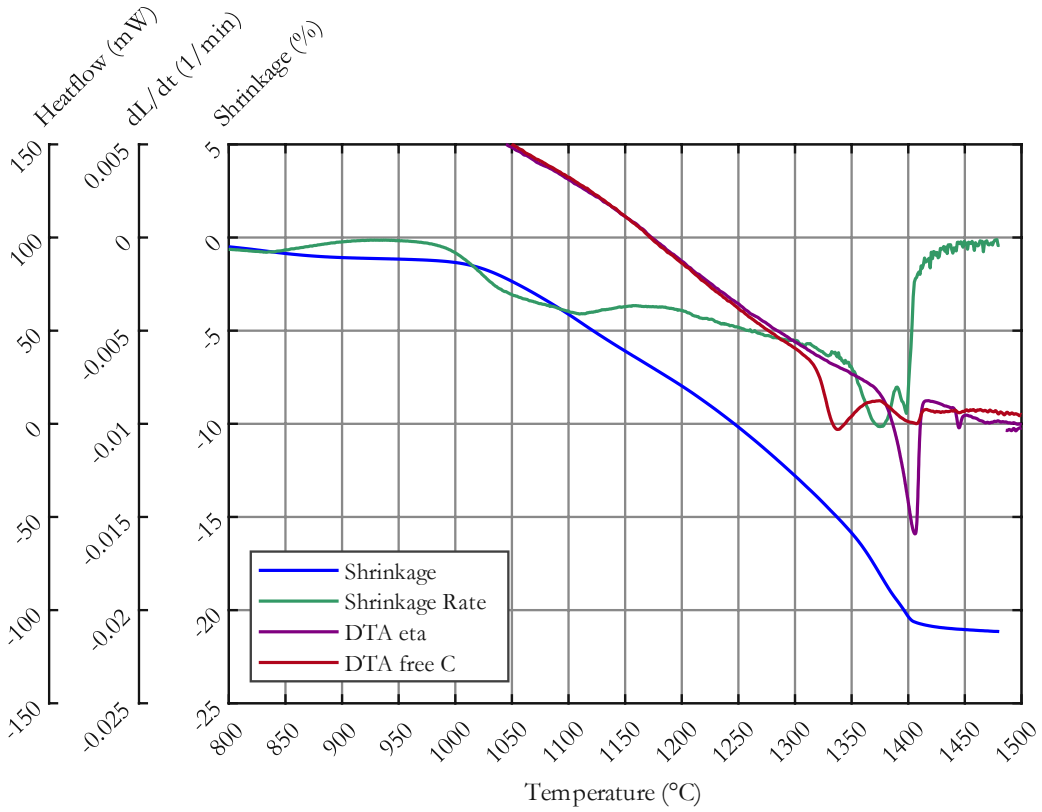

Figure 7-26: Combined diagram of dilatometer and DTA plotted against the temp. of sample 2D

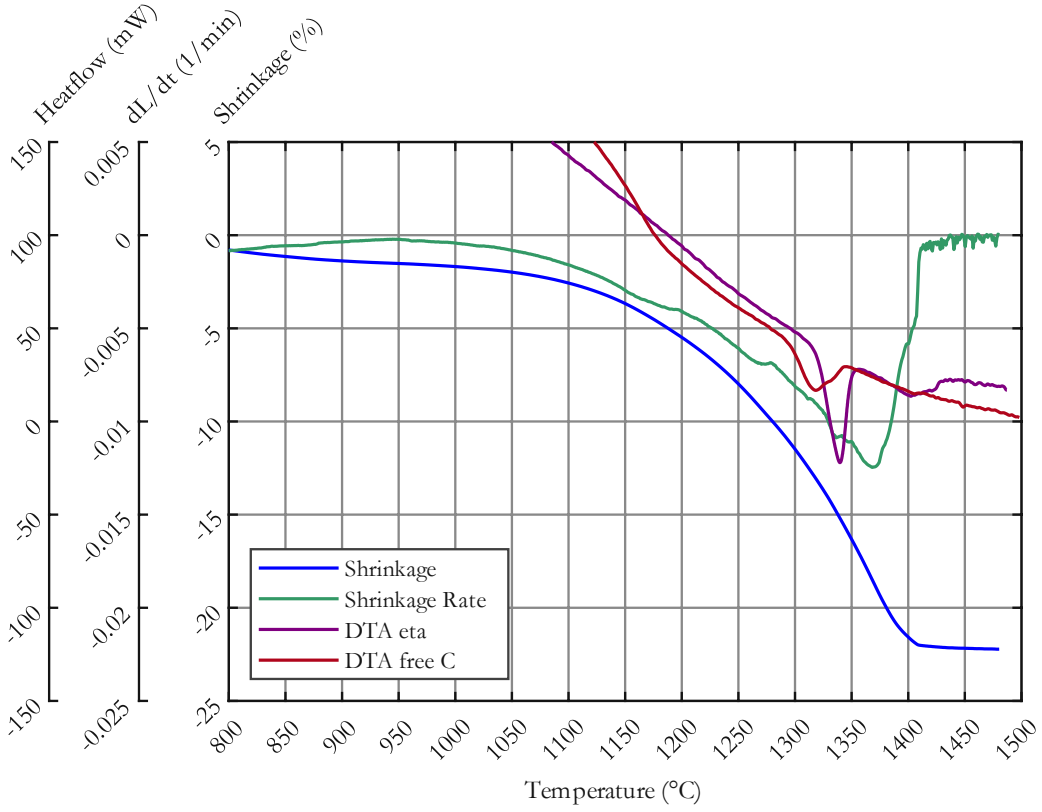

Figure 7-27: Combined diagram of dilatometer and DTA plotted against the temp. of sample 3A

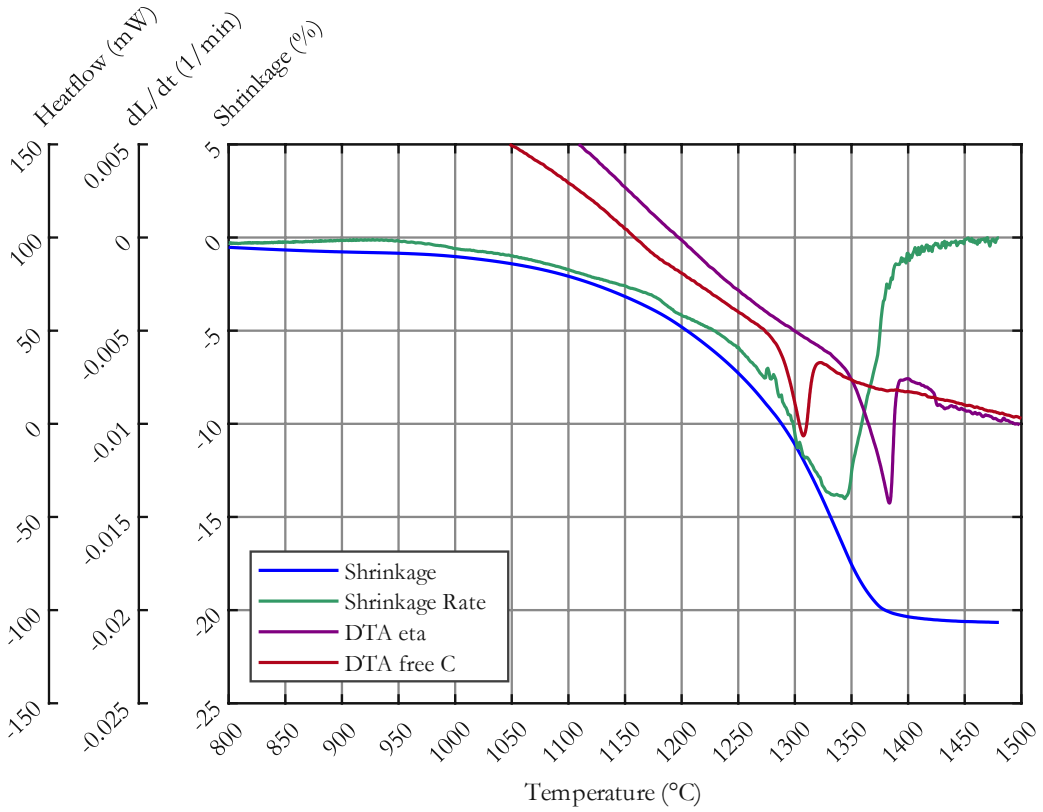

Figure 7-28: Combined diagram of dilatometer and DTA plotted against the temp. of sample 3B

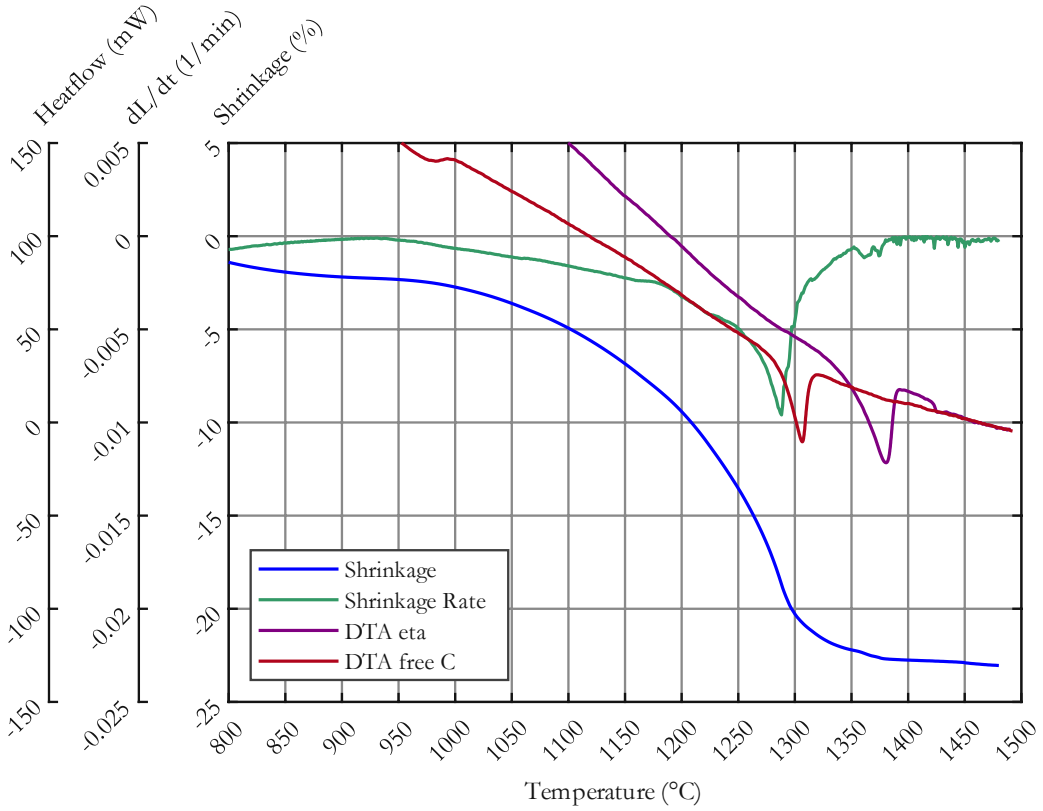

Figure 7-29: Combined diagram of dilatometer and DTA plotted against the temp. of sample 3C

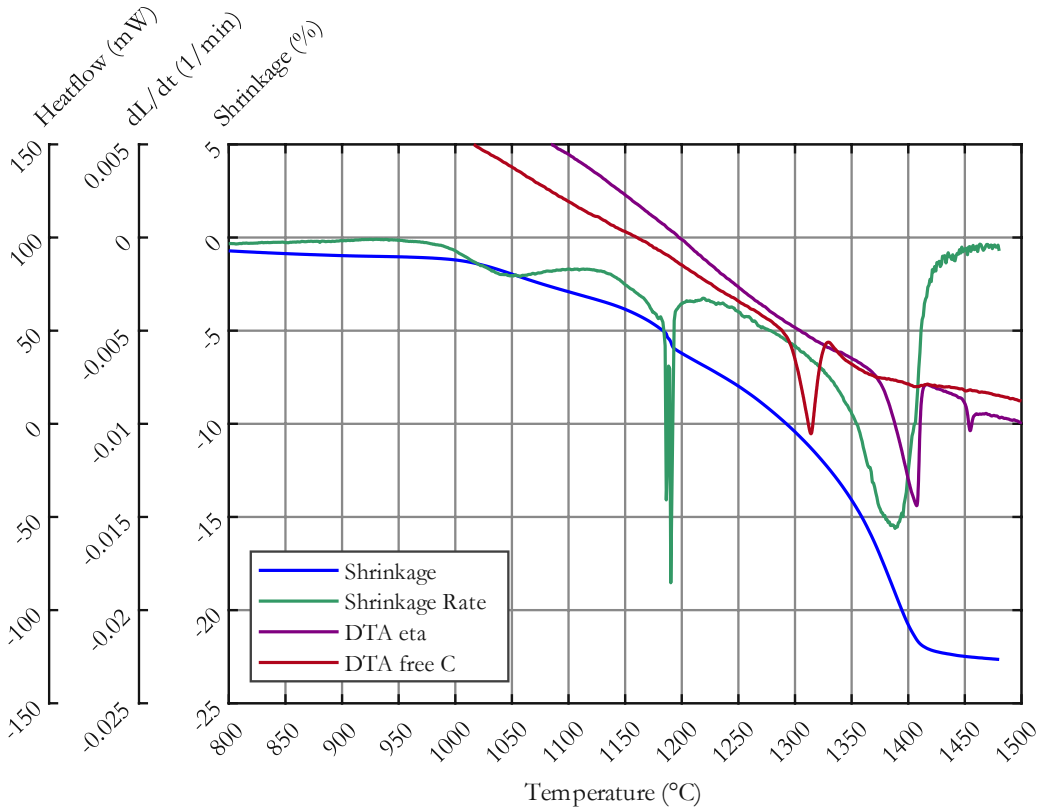

Figure 7-30: Combined diagram of dilatometer and DTA plotted against the temp. of sample 3D

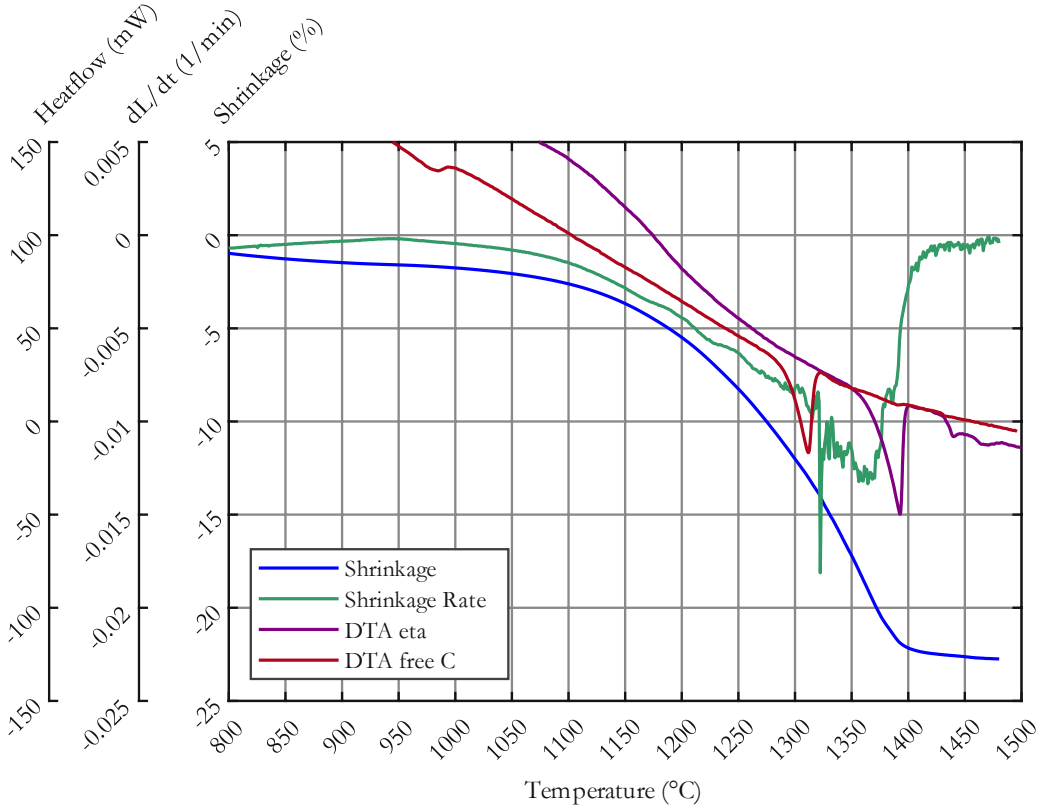

Figure 7-31: Combined diagram of dilatometer and DTA plotted against the temp. of sample 4A

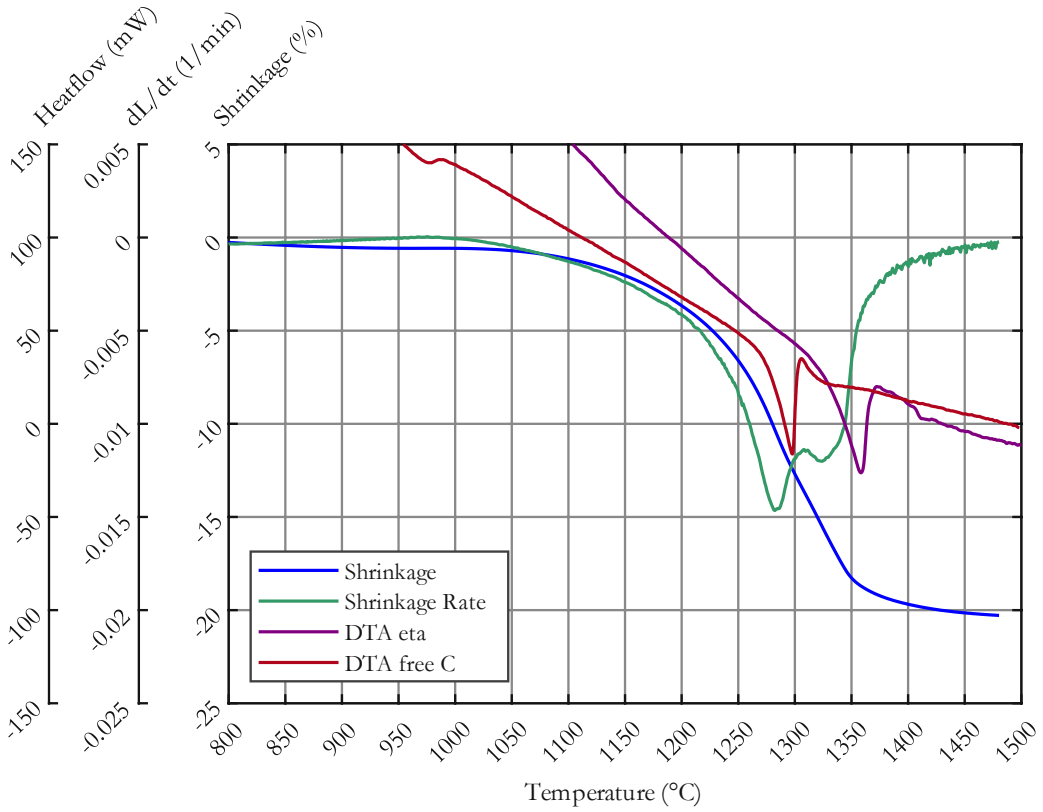

Figure 7-32: Combined diagram of dilatometer and DTA plotted against the temp. of sample 4B

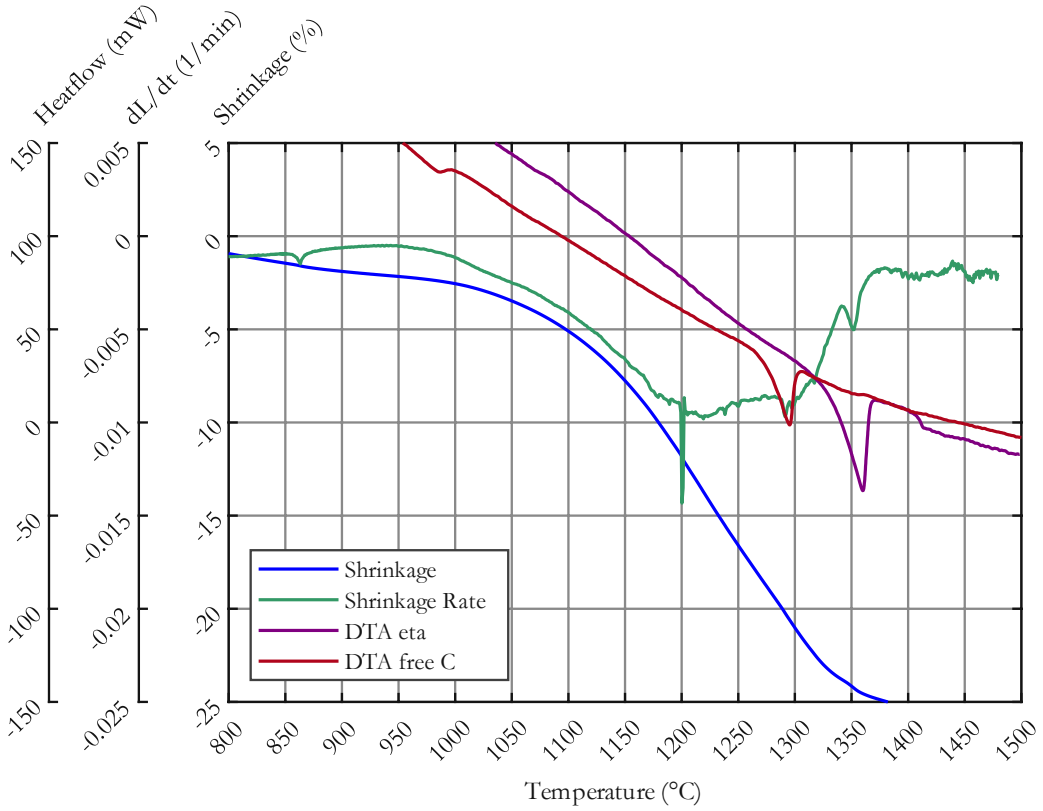

Figure 7-33: Combined diagram of dilatometer and DTA plotted against the temp. of sample 4C

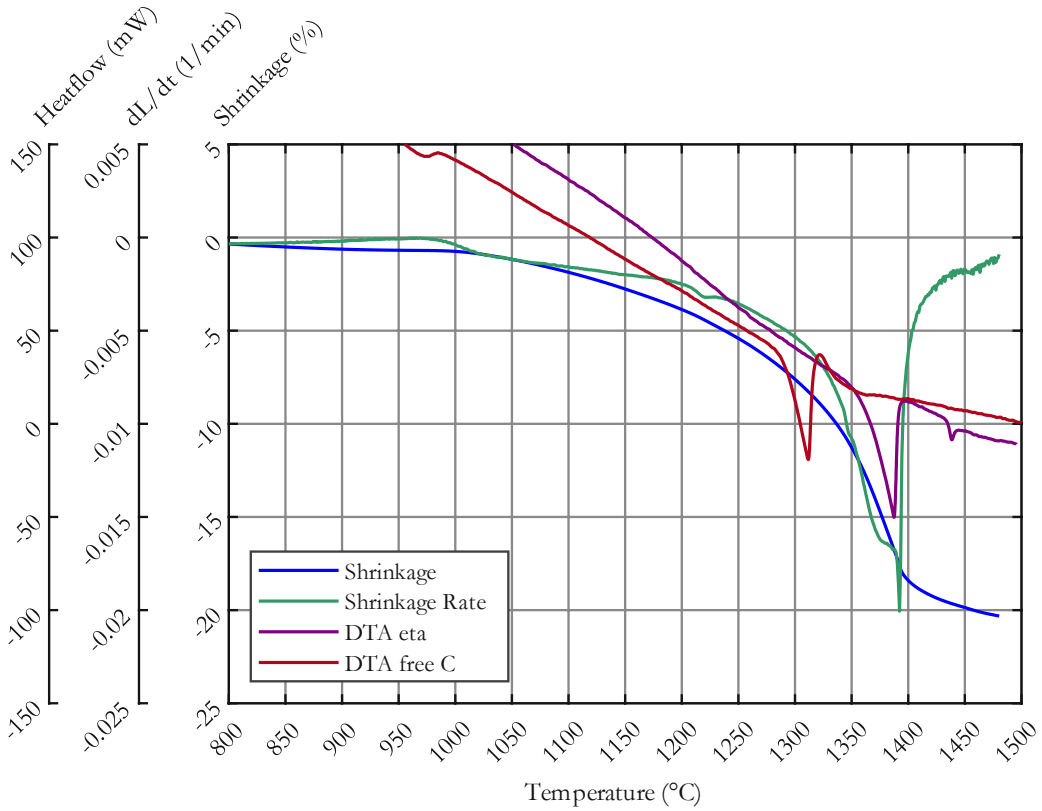

Figure 7-34: Combined diagram of dilatometer and DTA plotted against the temp. of sample 4D